TWO DIMENSIONAL IMMERSED BOUNDARY SIMULATIONS OF SWIMMING JELLYFISH

by

Haowen Fang

B.Eng., Nanjing University of Science and Technology, 2006

A Thesis submitted in partial fulfillment
of the requirements for the degree of

Master of Science

in the
Department of Mathematics
Faculty of Science

SIMON FRASER UNIVERSITY
Spring 2013

APPROVAL

Name: Haowen Fang

Degree: Master of Science

Title of Thesis: Two Dimensional Immersed Boundary Simulations Of Swimming Jellyfish

Examining Committee: Dr. Weiran Sun, Assistant Professor
Chair

Dr. John Stockie
Senior Supervisor
Associate Professor

Dr. Steven Ruuth
Supervisor
Professor

Dr. Nilima Nigam
Internal Examiner
Associate Professor

Date Approved: February 26, 2013.

Partial Copyright Licence

Abstract

The swimming behavior of jellyfish, driven by the periodic contraction of body muscles, can be modeled using a two dimensional bell-shaped membrane immersed in fluid with a periodic contraction force exerted along the membrane. We aim to use a simple two dimensional elastic membrane to simulate the swimming behavior without imposing any given membrane configuration, in which the swimming behavior is driven naturally by the interaction between the elastic membrane and fluid and solved by the immersed boundary (IB) method.

We begin by describing our implementation of stretching and bending forces in the IB formulation, and then study the relative importance of the stretching and bending forces for an idealized closed membrane. We then develop a two dimensional model of a jellyfish whose bell resists any deformation from a given target shape. The swimming dynamics are driven by a muscle contraction force that is fit to experimental data. Numerical simulations demonstrate an emergent swimming behavior that is consistent with experimentally observed jellyfish.

To my family
for their endless love and support.

"A journey of a thousand miles must begin with a single step."

— *Lao-tzu*

Acknowledgments

It's a long journey, and a great journey. I would like to thank my senior supervisor Dr. John Stockie for sailing me through this wonderful unknown territory, and inspiring me with his passion and professionalism during the past two years. I am very lucky to have him as my supervisor, and this thesis would not have been possible without his guidance and encouragement, especially his insights in academia. I would also like to thank all the professors for offering me excellent courses in this program, particularly Dr. Steve Ruuth, Dr. Razvan Fetecau and Dr. Ralf Wittenberg. I also want to thank all the members of the CFD group and PIMS for sharing an amazing academic atmosphere. Finally, I would like to express my special gratitude to my family and friends, especially my parents, for their endless support and love, which are the greatest asset in my life.

Contents

List of Tables

List of Figures

Chapter 1

Introduction

The immersed boundary (IB) method was proposed by C.S. Peskin [21] to solve problems involving fluid-structure interaction, in which an elastic structure or a membrane is immersed in a viscous incompressible fluid. The term "immersed boundary method" is used to refer to both a mathematical formulation and a numerical scheme. The IB method uses an Eulerian grid to denote the fluid domain and a Lagrangian grid to track the moving structure. The fluid-structure interaction is achieved by distributing the elastic forces generated by the structure onto neighboring fluid particles using delta functions. Then the distributed forces are applied to the fluid to update the fluid velocity and pressure, and finally the position of the structure is updated.

The IB method has many applications, such as blood flow around heart valves [9] and swimming animals in bio-fluid systems [4]. One well documented application is simulating the swimming motion of jellyfish. Figure 1.1 shows representative examples of six species jellyfish, including tentacles that extend from the edges of the bell and the flow patterns around their bodies.

Jellyfish swim by periodically contracting the bell muscle. A common approach to modeling jellyfish motion is to simplify the three dimensional jellyfish by considering a reduced two dimensional model consisting of a radial cross-section of the bell. Hamlet et al. [11] and Santhanakrishnan [12] studied the feeding behavior of an upside-down jellyfish, in which the jellyfish is adhered to a surface and so there is no actual locomotion taking place. Herschlag and Miller [13] developed a two dimensional model for a swimming jellyfish in which the configuration and location of the bell at each time step was given by a prescribed target

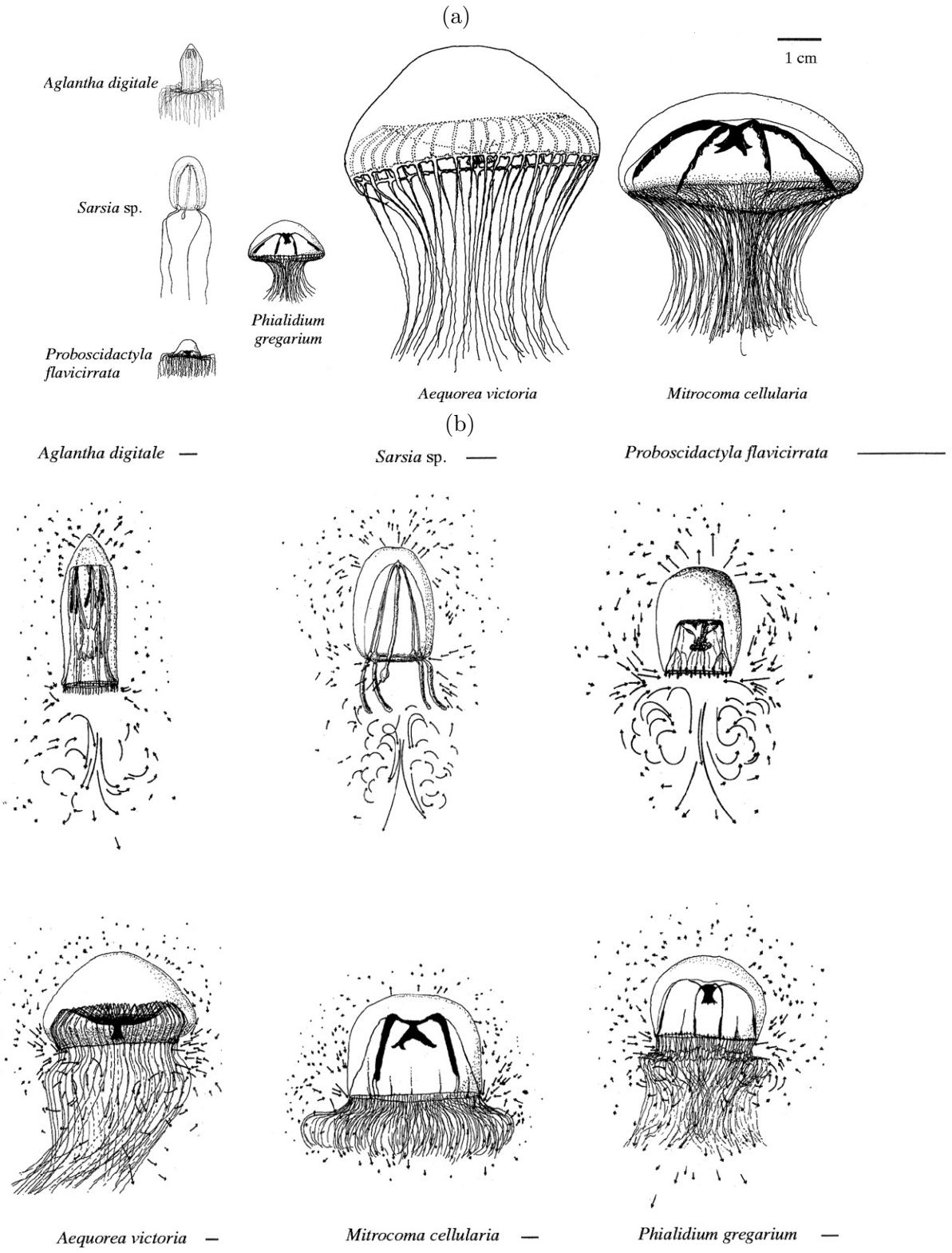

Figure 1.1: (a) Representative examples of jellyfish species. (b) Flow patterns around jellyfish. Reprinted with permission from *Springer Science and Business Media*[3, Figs. 1 and 7].

shape and the bell contraction force was not included. Rudolf [23] developed a three dimensional immersed boundary model of a swimming jellyfish, again for a prescribed IB motion – his approach was that of a computer animator in which video motion capture was used to determine the jellyfish location and the aim was to accurately simulate the fluid motion but not the fluid-structure interaction. Huang and Sung [14] developed a two dimensional IB model in which they included a given time dependent muscle contraction force in the bell model. Although this model contains more biophysical properties of the jellyfish, no comparisons with experimental data are performed. There are also many other numerical methods that have been applied to simulate swimming jellyfish, including the Arbitrary Lagrangian-Euler method [24], the penalization method [1], and the viscous vortex particle method [26] which uses the finite-time Lyapunov exponent field to reveal flow structures.

The purpose of this thesis is to establish a simple two dimensional jellyfish model based on experimental data from [3], and to capture the fundamental swimming dynamics, while removing any unnecessary complexity in the bell configuration. Our approach is close to that of Huang and Sung [14] in that we do not impose any particular location or shape to the bell over time. Instead, we specify only an "equilibrium shape" for the bell and the time dependent behaviors of the swimming muscles, and then compare the emergent swimming dynamics of our computational jellyfish to experimental measurements.

In Chapter 2, we first introduce the background information about the immersed boundary method and the stretching and bending forces needed to model the bell muscle. Chapter 3 provides a series of simulations for the oscillation of an idealized closed membrane under the effects of different combinations of stretching force and bending force, and we identify the relative importance of the stretching and bending effects on the membrane. In Chapter 4, two simulations are presented that verify the stretching force and bending force calculations in an open, bell-shaped membrane simulation, and then a two dimensional jellyfish model is established based on the jellyfish species considered in [3]. Simulations are compared with the experimental data from [3].

Chapter 2

The Immersed Boundary Method

The immersed boundary (IB) method was first introduced by Peskin [21] to simulate the interaction between the heart muscle and the blood in which it is immersed. The IB method is a mathematical formulation as well as a numerical scheme. If we simplify the model in a two dimensional geometry, a surface is often replaced by a one dimensional fibre or membrane immersed in a two dimensional domain filled with fluid. The fibre is assumed to be massless, neutrally buoyant and have zero volume.

2.1 Mathematical Formulation by Delta Functions

An Eulerian description is used for the square fluid domain denoted as $\Omega = [0,1] \times [0,1]$, where an arbitrary point in the fluid domain is defined as $\boldsymbol{x} = (x, y)$. The fibre on the other hand is described as

$$\boldsymbol{X}(s,t) = (X(s,t), Y(s,t)), \tag{2.1}$$

for any time t, where s is a Lagrangian coordinate that parameterizes points on the fiber. Figure 2.1 pictures two types of fibres immersed in the fluid domain, in which Γ_1 denotes a closed fibre and Γ_2 denotes an open fibre.

The motion of the fluid is governed by the incompressible Navier-Stokes equations

$$\begin{aligned} \rho \frac{\partial \boldsymbol{u}}{\partial t} + \rho \boldsymbol{u} \cdot \nabla \boldsymbol{u} &= \mu \Delta \boldsymbol{u} - \nabla p + \boldsymbol{f}, \\ \nabla \cdot \boldsymbol{u} &= 0, \end{aligned} \tag{2.2}$$

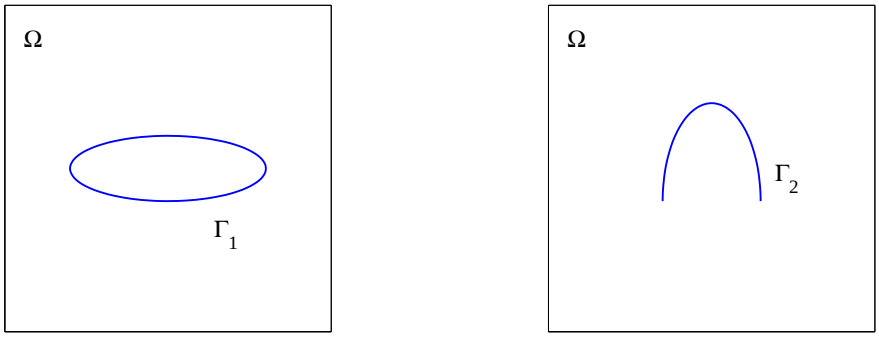

Figure 2.1: Closed fibre, Γ_1, and open fibre, Γ_2, immersed in the fluid domain, $\Omega : [0,1] \times [0,1]$.

where $\boldsymbol{u}(\boldsymbol{x},t) = (u(\boldsymbol{x},t), v(\boldsymbol{x},t))$ is the fluid velocity $[cm \cdot s^{-1}]$, $p(\boldsymbol{x},t)$ is the pressure $[g \cdot cm \cdot s^{-2}]$, $\boldsymbol{f}(\boldsymbol{x},t)$ is the fluid volumetric force $[g \cdot cm^{-2} \cdot s^{-2}]$, ρ $[g \cdot cm^{-3}]$ is the fluid density and μ $[g \cdot cm^{-1} \cdot s^{-1}]$ is dynamic viscosity.

The membrane is neutrally buoyant in the fluid, so that gravity is negligible. Thus the force f in the Navier-Stokes equations arises solely from the fibre elastic force, which consists of two effects: a bending-resistant force and a stretching-resistant force. These IB forces are actually specified in terms of a force density on the immersed boundary (a force per unit length), where the total force density from bending and stretching is written as

$$\boldsymbol{F}(s,t) = \boldsymbol{F}_b(s,t) + \boldsymbol{F}_s(s,t). \tag{2.3}$$

The elastic force density is applied only to the fluid that is at the same location as fibre points, so that the fluid force $\boldsymbol{f}$ can be written as an integral of the total IB force density along the fibre Γ

$$\boldsymbol{f}(\boldsymbol{x},t) = \int_\Gamma \boldsymbol{F}(s,t)\delta(\boldsymbol{x} - \boldsymbol{X}(s,t))ds, \tag{2.4}$$

where the two dimensional delta function is the product of two one dimensional delta functions, $\delta(\boldsymbol{x}) = \delta(x) \cdot \delta(y)$.

Due to the no-slip condition, the fibre moves at the same velocity as neighboring fluid points, and this yields the equation

$$\frac{\partial \boldsymbol{X}}{\partial t} = \boldsymbol{u}(\boldsymbol{X}(s,t),t) = \int_\Omega \boldsymbol{u}(\boldsymbol{x},t)\delta(\boldsymbol{x} - \boldsymbol{X}(s,t))d\boldsymbol{x}. \tag{2.5}$$

In summary, the dynamics of the fluid-fibre system can be described by the following coupled equations:

$$\begin{aligned} \rho\frac{\partial \boldsymbol{u}}{\partial t} + \rho\boldsymbol{u}\cdot\nabla\boldsymbol{u} &= \mu\Delta\boldsymbol{u} - \nabla p + \int_\Gamma \boldsymbol{F}(s,t)\delta(\boldsymbol{x}-\boldsymbol{X}(s,t))ds, \\ \nabla\cdot\boldsymbol{u} &= 0, \\ \frac{\partial \boldsymbol{X}}{\partial t} &= \int_\Omega \boldsymbol{u}(\boldsymbol{x},t)\delta(\boldsymbol{x}-\boldsymbol{X}(s,t)))d\boldsymbol{x}. \end{aligned} \tag{2.6}$$

The only remaining detail is the IB force density $\boldsymbol{F}$ which is described in the next section.

2.2 Immersed Fibre with Stretching and Bending Forces

Due to stretching and bending effects generated by the solid material properties, the immersed fibre exerts forces on the surrounding fluid. The direction and magnitude of these forces are dependent on the difference between the current configuration and a given target configuration of the solid material. The immersed fibre is modeled as a curve with points identified by a Lagrangian parameter $s \in [0,1]$.

In this thesis, we consider a fibre that resists stretching (or compression) and bending. The stretching force is written in terms of the tension in the fibre, which can be expressed as a function of the fibre strain:

$$\boldsymbol{T}(s,t) = \boldsymbol{T}\left(\left|\frac{\partial \boldsymbol{X}(s,t)}{\partial s}\right|\right), \tag{2.7}$$

where $\boldsymbol{X}(s,t)$ represents the location of the membrane points with parametrization s at an arbitrary time t.

The fibre is assumed to be a Hookean material, so that the tension force is proportional to strain. If the fibre has an equilibrium configuration that satisfies $\left|\frac{\partial \boldsymbol{X}(s,t)}{\partial s}\right| = R$ for some positive constant R then a simple linear Hookean relation for the tension force is

$$\boldsymbol{T}(s,t) = \sigma_s\left(\left|\frac{\partial \boldsymbol{X}}{\partial s}\right| - R\right), \tag{2.8}$$

where σ_s $[g/cm^2]$ is the "spring constant" of the fibre. The local stretching force density per unit length is given by

$$\boldsymbol{F}_s(s,t) = \frac{\partial(\boldsymbol{T}\tau)}{\partial s}, \tag{2.9}$$

where the unit tangent vector to the fiber at a given point is

$$\tau = \frac{\frac{\partial \boldsymbol{X}}{\partial s}}{\left|\frac{\partial \boldsymbol{X}}{\partial s}\right|}. \tag{2.10}$$

Combining equations (2.8),(2.9) and (2.10), we obtain:

$$\boldsymbol{F}_s(s,t) = \sigma_s \frac{\partial}{\partial s}\left[\frac{\partial \boldsymbol{X}(s,t)}{\partial s}\left(1 - \frac{R}{\left|\frac{\partial \boldsymbol{X}(s,t)}{\partial s}\right|}\right)\right]. \tag{2.11}$$

The bending resistant force has a different form. If the membrane is bent away from an equilibrium configuration, elastic energy is generated and can be written in the form [9]

$$E_b(\boldsymbol{X},t) = \frac{1}{2}\int_\Omega \sigma_b \left|\frac{\partial^2 \boldsymbol{X}}{\partial s^2} - \frac{\partial^2 \boldsymbol{X}^0}{\partial s^2}\right|^2 ds, \tag{2.12}$$

where σ_b $[g/cm^4]$ is a bending stiffness parameter that is a constant along the fibre, and $\boldsymbol{X}^0$ is the fibre equilibrium configuration, which we also call the "target configuration". The bending force density can be expressed as the variational derivative

$$\boldsymbol{F}_b(s,t) = -\frac{\delta E_b(\boldsymbol{X},t)}{\delta \boldsymbol{X}}, \tag{2.13}$$

which is equivalent to

$$\boldsymbol{F}_b(s,t) = \sigma_b\left(\frac{\partial^4 \boldsymbol{X}^0}{\partial s^4} - \frac{\partial^4 \boldsymbol{X}}{\partial s^4}\right). \tag{2.14}$$

This equation ensures that as the fibre approaches the equilibrium configuration, the bending force density approaches zero, and the steady state of the fibre has the same curvature as the equilibrium configuration.

2.3 Numerical Scheme

There are many different numerical approaches for implementing the immersed boundary method, and we use the method described in [25] which is essentially the original method proposed by Peskin.

The immersed boundary method uses a fixed Eulerian grid to discretize the fluid, and a moving Lagrangian grid to describe the fibre. The fluid points are labeled as $\boldsymbol{x}_{i,j} = (x_i, y_j) = (ih, jh)$ on a fixed $N \times N$ grid, with spacing $h = \frac{1}{N}$ in both directions. The fluid domain

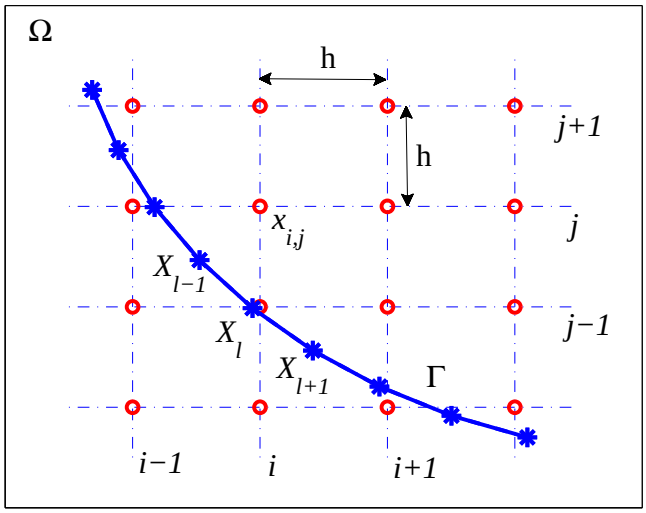

Figure 2.2: Discretization of an immersed fibre in a square fluid domain, $\Omega : [0,1] \times [0,1]$.

has doubly-periodic boundary conditions so that x_0 and x_N are identical, as are y_0 and y_N[1]. The fibre is discretized on a Lagrangian grid with N_b equally spaced points, with $s_l = l \cdot h_b$ and $h_b = \frac{1}{N_b}$. The fluid and fibre points share the same equally-spaced time $t_n = n \cdot \Delta t$, where Δt is the time step. Figure 2.2 shows the square fluid domain and the immersed fibre, where "$\circ$" represent fluid points and "$*$" represent fibre points. The velocity, pressure and force at an arbitrary fluid point $\boldsymbol{x}_{i,j}$ and time t_n have discrete approximations:

$$\boldsymbol{u}^n_{i,j} \approx \boldsymbol{u}(x_i, y_j, t_n)$$
$$p^n_{i,j} \approx p(x_i, y_j, t_n)$$
$$\boldsymbol{f}^n_{i,j} \approx \boldsymbol{f}(x_i, y_j, t_n)$$

where $i, j = 0, 1, 2, ..., N-1$, and $n = 0, 1, 2, ...$ The fibre location and force density at the Lagrangian point l and time t_n can be expressed as

$$\boldsymbol{X}^n_l \approx \boldsymbol{X}(s_l, t_n),$$
$$\boldsymbol{F}^n_l \approx \boldsymbol{F}(s_l, t_n),$$

[1]It is important to note that the periodic boundary conditions are imposed as a matter of convenience only, and that in any immersed boundary simulation we must take care to choose a large enough domain size that the interference between periodic copies of the immersed boundary is minimized.

where $l = 0, 1, 2, ..., N_b$, and $n = 0, 1, 2, ...$

The two dimensional delta function in equations (2.4),(2.5),(2.6) is the product of two one dimensional delta functions $\delta(\boldsymbol{x}) = \delta(x) \cdot \delta(y)$, so that a given point $\boldsymbol{x}_{i,j} = (x_i, y_j)$, the product can be expressed as:

$$\delta(\boldsymbol{x}_{i,j}) = \delta_h(x_i, y_j) = d_h(x_i) \cdot d_h(y_j).$$

In computations, the one dimensional delta function is approximated by

$$d_h(x) = \begin{cases} \frac{1}{4h}\left(1 + \cos\frac{\pi x}{2h}\right), & |x| < 2h, \\ 0, & |x| \geq 2h. \end{cases} \tag{2.15}$$

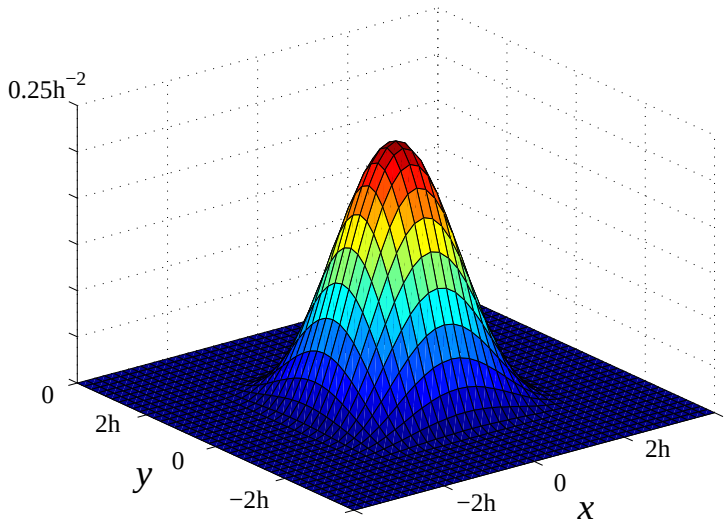

Figure 2.3: The cosine approximation $\delta_h(x, y)$ to the delta function.

This discrete delta function has finite support so that the fibre points only interact with a few neighboring fluid points, which keeps the computational cost at a reasonable level. Figure 2.3 illustrates the approximation of the two dimensional delta function.

In order to simplify notation in the numerical scheme, the notation from [25] is followed. On the Eulerian grid, $\phi^n_{i,j}$ denotes the value of the function $\phi(x)$ evaluated at point $\boldsymbol{x}_{i,j} = (ih, jh)$ at time t_n. Similarly, ψ^n_l denotes the value of the function ϕ evaluated at the Lagrangian point $s_l = lh_b$ at time t_n.

The following finite difference operators are used on the Eulerian grid:

• First-order derivative approximation by one-sided differences

$$D_x^+\phi_{i,j} = \frac{\phi_{i+1,j} - \phi_{i,j}}{h},$$
$$D_x^-\phi_{i,j} = \frac{\phi_{i,j} - \phi_{i-1,j}}{h},$$
$$D_y^+\phi_{i,j} = \frac{\phi_{i,j+1} - \phi_{i,j}}{h},$$
$$D_y^-\phi_{i,j} = \frac{\phi_{i,j} - \phi_{i,j-1}}{h};$$

• Second-order derivative approximations of the first derivative

$$D_x^0\phi_{i,j} = \frac{\phi_{i+1,j} - \phi_{i-1,j}}{2h},$$
$$D_y^0\phi_{i,j} = \frac{\phi_{i,j+1} - \phi_{i,j-1}}{2h};$$

• The discrete gradient

$$\nabla_h\phi_{i,j} = (D_x^0, D_y^0)\phi_{i,j},$$

and Laplacian

$$\Delta_h\phi_{i,j} = (D_x^+D_x^+ + D_y^+D_y^+)\phi_{i,j}.$$

If we apply analogous differences on the Lagrangian grid, the one-side first-order derivative operators are

$$D_s^+ = \frac{\psi_{l+1} - \psi_l}{h_b},$$
$$D_s^- = \frac{\psi_l - \psi_{l-1}}{h_b}.$$

Assuming that at time $t_{n-1} = (n-1)\Delta t$, the fluid velocity and fibre position are known as $\boldsymbol{u}_{i,j}^{n-1}$ and $\boldsymbol{X}_{i,j}^{n-1}$, the solutions at time $t = n\Delta t$ are determined as follows:

(1) Compute the total fibre force density $\boldsymbol{F}$ using the fibre position $\boldsymbol{X}_{i,j}^{n-1}$

$$\boldsymbol{F}_l^{n-1} \cong \boldsymbol{F}(\boldsymbol{X}_l^{n-1}) = \boldsymbol{F}_s(\boldsymbol{X}_l^{n-1}) + \boldsymbol{F}_b(\boldsymbol{X}_l^{n-1}).$$

Apply the notation:

$$\begin{aligned}\boldsymbol{F}_l^{n-1} \approx \sigma_s D_s^- \left[(D_s^+\boldsymbol{X}_l^{n-1})\left(1 - \frac{R}{|D_s^+\boldsymbol{X}_l^{n-1}|}\right)\right] \\ + \sigma_b D_s^+ D_s^- \left(D_s^+ D_s^- \boldsymbol{X}_l^0 - D_s^+ D_s^- \boldsymbol{X}_l^{n-1}\right).\end{aligned} \tag{2.16}$$

(2) Distribute the force to neighboring fluid points:

$$\boldsymbol{f}_{i,j}^{n-1} = \sum_{l=1}^{N_b} \boldsymbol{F}_l^{n-1} \delta_h(\boldsymbol{x}_{i,j} - \boldsymbol{X}_l^{n-1}) \cdot h_b. \tag{2.17}$$

(3) Solve the Navier-Stokes equations using a split-step projection scheme:

(a) Use an alternating direction implicit (ADI) method to apply the force, convection and diffusion terms:

$$\begin{aligned} \rho\left(\frac{\boldsymbol{u}_{i,j}^{n,0} - \boldsymbol{u}_{i,j}^{n-1}}{\Delta t}\right) &= \boldsymbol{f}_{i,j}^{n-1}, \\ \rho\left(\frac{\boldsymbol{u}_{i,j}^{n,1} - \boldsymbol{u}_{i,j}^{n,0}}{\Delta t} + u_{i,j}^{n-1} D_x^0 \boldsymbol{u}_{i,j}^{n,1}\right) &= \mu D_x^+ D_x^- \boldsymbol{u}_{i,j}^{n,1}, \\ \rho\left(\frac{\boldsymbol{u}_{i,j}^{n,2} - \boldsymbol{u}_{i,j}^{n,1}}{\Delta t} + v_{i,j}^{n-1} D_y^0 \boldsymbol{u}_{i,j}^{n,2}\right) &= \mu D_y^+ D_y^- \boldsymbol{u}_{i,j}^{n,2}, \end{aligned} \tag{2.18}$$

where velocity $\boldsymbol{u} = (u, v)$has two components in the convection terms. $\boldsymbol{u}_{i,j}^{n,0}$ has an explicit form, while $\boldsymbol{u}_{i,j}^{n,1}$ and $\boldsymbol{u}_{i,j}^{n,2}$ are two intermediate velocities, that both require solving tridiagonal linear systems.

(b) Use Chorin's projection method to determine pressure and velocity at the next time step:

$$\begin{aligned} \rho\left(\frac{\boldsymbol{u}_{i,j}^{n} - \boldsymbol{u}_{i,j}^{n,2}}{\Delta t}\right) + \nabla_h p_{i,j}^n &= 0, \\ \nabla_h \cdot \boldsymbol{u}_{i,j}^n &= 0. \end{aligned} \tag{2.19}$$

After applying the discrete gradient to (2.19), the pressure equation becomes:

$$\Delta_{2h} p_{i,j}^n = \frac{\rho}{\Delta t} \cdot \boldsymbol{u}_{i,j}^{n,2}, \tag{2.20}$$

where $\Delta_{2h} = \nabla_h \cdot \nabla_h$ is a wide (2h-spaced) finite difference operator for the Laplacian. We solve the pressure Poisson equation with a Fast Fourier Transform (FFT), then use the updated pressure to get the velocity at the next time step:

$$\boldsymbol{u}_{i,j}^n = \boldsymbol{u}_{i,j}^{n,2} - \frac{\Delta t}{\rho} \nabla_h p_{i,j}^n. \tag{2.21}$$

(4) Use the velocity $\boldsymbol{u}_{i,j}^n$ to update the fibre position:

$$\boldsymbol{X}_l^n = \boldsymbol{X}_l^{n-1} + h^2 \Delta t \sum_{i,j=1}^{N} \boldsymbol{u}_{i,j}^n \delta_h(\boldsymbol{x}_{i,j} - \boldsymbol{X}_l^{n-1}). \tag{2.22}$$

The above 4-step procedure is the complete scheme to update the fluid and fibre variables from one time step to the next. The IB method is first order in time and formally second order accurate in space, but the use of the discrete delta function reduces the spatial accuracy to first order [20]. This scheme is flexible in the fibre geometry, but can have a severe time step restriction because of the explicit treatment of the fibre force, as observed in [25]. The stability restriction for the IB method has been derived by Boffi et al. [2], who applied energy estimates to a variational form of the governing equations. Their time step restriction can be written as $\Delta t \leq Kh/\sigma$, where σ represents the size of the IB force and K is a constant that depends on the problem geometry and other numerical parameters. In our simulations, we find that we must also impose a time step restriction that is consistent with that of Boffi et al.

Chapter 3

Simulation of a Closed Membrane

In this chapter, we apply the immersed boundary method described in Chapter 2 to study the motion of a closed, elastic membrane immersed in fluid, where the elastic force derives from two effects: stretching resistant forces and bending resistant forces. We begin by describing the model set-up and then perform a series of simulations to analyze the effects of stretching and bending forces. These simulations are divided into three cases, stretching force only, bending force only, and a combination of stretching and bending forces, which we refer to as cases 1, 2 and 3 respectively. We compare the effects of stretching and bending forces in case 3, and draw conclusions regarding the two forcing effects. The purpose of this chapter is to determine the relative importance of the stretching and bending effects in the simple case of a closed membrane, which will guide us in selecting forcing parameters for our jellyfish simulations. We note that in the jellyfish simulations, the stretching force is an artificial force whose purpose is to maintain a (nearly) constant length of the bell.

3.1 An Elliptical Immersed Membrane

We consider a membrane immersed in a two dimensional square fluid domain, pictured in Figure 3.1. The fluid domain is defined as $\Omega = [0,1] \times [0,1]$, and the membrane is a closed fibre Γ, with fluid both inside and outside. The fluid domain Ω has periodic boundary conditions in both the $x-$ and $y-$ directions. The membrane is defined using a Lagrangian parameter $s \in [0,1]$, and the initial configuration is an ellipse under tension. In the simplest case, with stretching force only, the equilibrium configuration is a circle that represents a balance between the pressure of the fluid inside the membrane and the tension force in the

membrane itself. When a non-uniform bending force is added later, then the equilibrium shape can be non-circular.

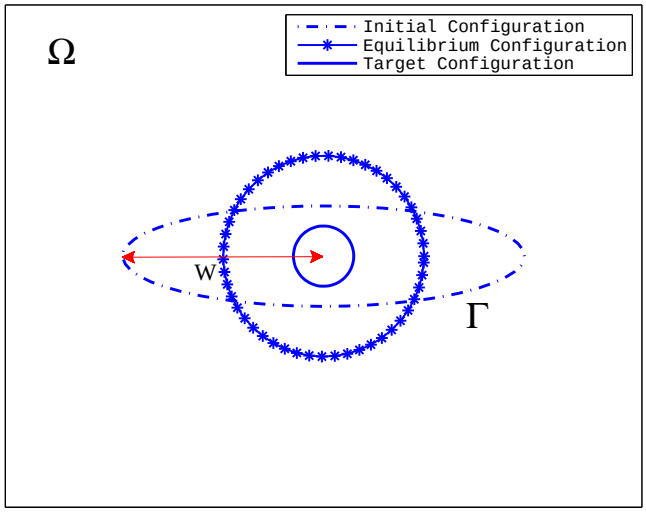

Figure 3.1: The two dimensional fluid domain, Ω, containing a closed elliptical fibre, Γ.

The membrane is an elastic and non-porous material, pictured in Figure 3.1, and the fluid is at rest initially. The target length of the membrane is set to be less than the initial length, so that the membrane is stretched at the beginning. As the simulation starts, elastic forces drive the membrane to oscillate around its equilibrium configuration, and the motion gradually damps out because of viscous effects. The distance between the center of the domain and the left most point on the membrane, indicated as "W" in the figure, and denoted as the $x-$width or horizontal width, is used as the indicator to show the magnitude of the oscillation. As a result of mass conservation, the equilibrium shape has the same area as the initial elliptical configuration, which we refer to as area conservation. The elliptical initial configuration is defined by the following equations:

$$\begin{cases} X(s) = x_0 + r_1 \cdot \cos(2\pi s), \\ Y(s) = y_0 + r_2 \cdot \sin(2\pi s), \end{cases} \tag{3.1}$$

where $\boldsymbol{X}(s) = (X(s), Y(s))$, (x_0, y_0) is the center of the ellipse, and r_1 and r_2 represent the semi-axes of the ellipse. The area of the initial ellipse is $\pi r_1 r_2$. If the equilibrium

configuration is a circle, the radius of the corresponding equilibrium circle is $r = \sqrt{r_1 \cdot r_2}$ according to area conservation. For the simulations in this chapter, we use $\rho = 1$ and $\mu = 1$ as the fluid density and dynamic viscosity respectively, and the initial membrane has semi-major and semi-minor axes $r_1 = 0.4$ and $r_2 = 0.1$ respectively. The area enclosed in this membrane is $\pi r_1 r_2 = 0.04\pi$.

3.2 Case 1: Stretching Force Only

We start by studying the oscillations caused by a stretching force, where the stretching stiffness parameter is denoted as σ_s. Recall the formula (2.11), for the stretching force with resting length R, which refers to the unstretched state for which the force is zero. If the stretching force is zero, $R = |\frac{\partial \boldsymbol{X}}{\partial s}|$, and this implies that the distance between consecutive membrane points is $|d\boldsymbol{X}| = R \cdot ds$. If we specify the membrane points to be equally spaced in the equilibrium state, then the equilibrium configuration is a circle. The membrane is non-porous and so due to the area conservation the area of membrane is the same as that of the elliptical initial configuration regardless of the equilibrium constant R.

In the following simulation, we set the resting length $R = 0$, so that the membrane is always under tension and use different values of stretching stiffness σ_s. The results in Figure 3.2 indicate that the oscillations damp out as the fibre approaches its circular equilibrium state with radius $r_{eq} = \sqrt{0.4 \cdot 0.1} = 0.2$. We plot the maximum horizontal width, which is defined previously as the distance between the left most point and the center of the membrane along $x-$ direction. It is used as an indicator of the magnitude of oscillation. The equilibrium radius r_{eq} is also shown as a dotted horizontal line for reference in Figure 3.2.

The results in Figure 3.2 indicate that as the stretching stiffness increases, the fibre oscillates at a higher frequency, but the oscillation damps out more quickly. This is consistent with the analytical results derived in [25] and [5]. For different σ_s values, fibres in the four cases of Figure 3.2 share the same initial stretch, so a larger σ_s yields a larger initial stretching force, resulting in a larger velocity and higher frequency. As the fibre oscillates at a higher speed, total energy damps out at a higher rate, and the oscillation damps out more rapidly as σ_s increases.

A more detailed picture is provided for the simulation with $\sigma_s = 2000$ in Figure 3.3. Here, the membrane attains a minimum width along the $x-$ direction at around $t = 0.005, t =$

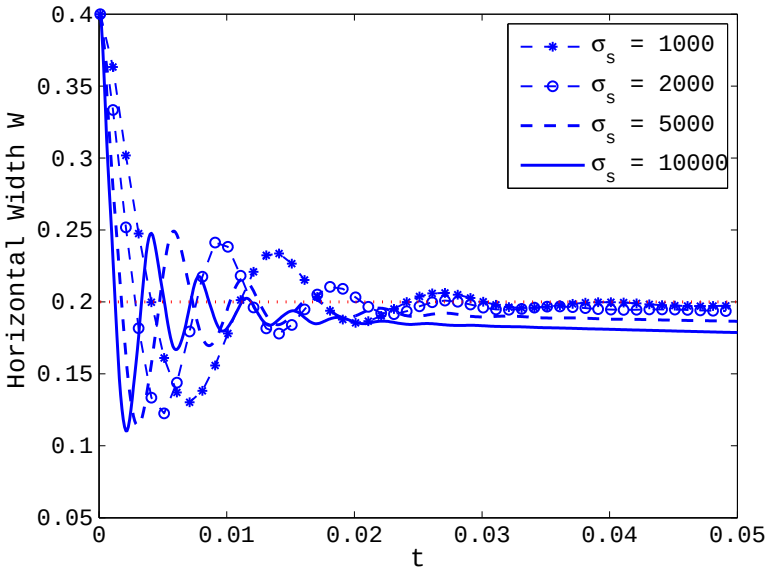

Figure 3.2: Case 1 (stretching only): Horizontal width for different σ_s. The equilibrium radius $r_{eq} = 0.2$ is shown as a dotted horizontal line.

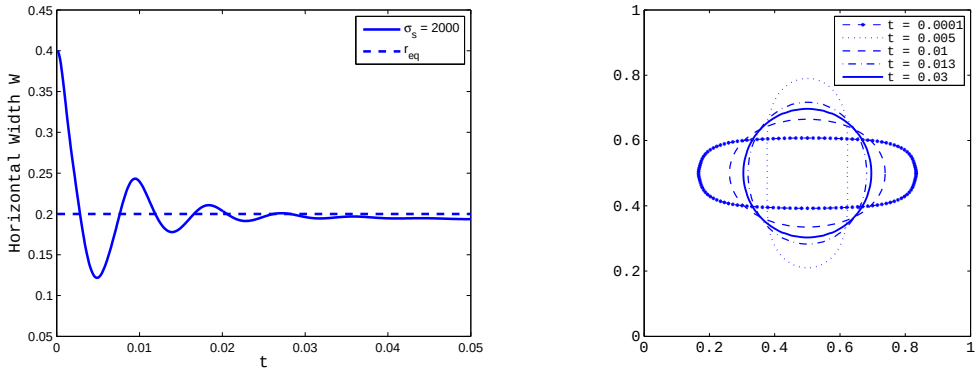

Figure 3.3: Case 1 (stretching only): Oscillation and profile of the fibre with $\sigma_s = 2000$.

0.015 and maximum width at around $t = 0.01, t = 0.02$, and then it settles into its circular equilibrium configuration. Figure 3.3 illustrates the configuration of the fibre at some important oscillation steps.

We also notice that the radius decreases very gradually over a long time after the membrane reaches its equilibrium configuration, which indicates that the area is shrinking even assuming the fibre is non-porous [22], [8]. This is a well documented phenomenon and is one of the disadvantages of IB method, arising from the fact that errors in the discrete divergence free condition lead to a gradual "leaking" of fluid out of the membrane. This effect can be reduced by taking a finer grid, or by implementing a volume-conserving divergence stencil advocated by Peskin and Printz [22]. Figure 3.4 shows the leaking effect with the three grid sizes $N = 32, N = 64, N = 128$ and $\sigma_s = 10^4$. This indicates that a refined grid reduces the leaking effect, but it is still significant.

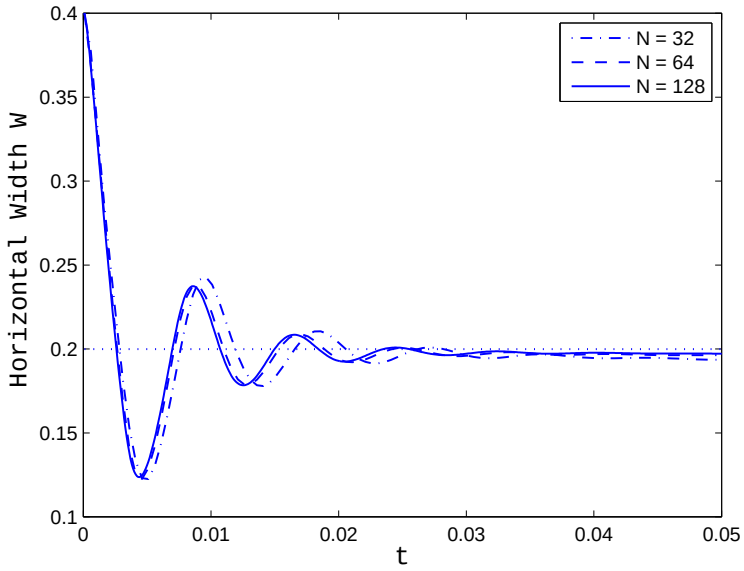

Figure 3.4: Case 1 (stretching only): Effect of area loss for different fluid grid spacings and $\sigma_s = 10^4$.

3.3 Case 2: Bending Force Only

In this section, we study the case where the membrane dynamics are driven solely by a bending force, as given in Equation (2.14). The membrane has bending stiffness σ_b, and otherwise we use the same parameters as in case 1. In case 1, the membrane eventually settled down to a circular configuration, whereas in case 2, the membrane settles down to different configurations depending on the target configuration $\boldsymbol{X}^0$. If $\boldsymbol{X}^0$ corresponds to a circular state or $\boldsymbol{X}^0 = 0$ (the latter of which we referred to as the case "without target configuration"), the membrane settles down to an equilibrium state that is circular. Otherwise, the membrane settles down to an equilibrium configuration that depends on $\boldsymbol{X}^0$ and is determined by a balance between the membrane bending force and the fluid forces deriving from the fluid inside the pressured membrane.

3.3.1 Bending Force Without Target Configuration

We test different values of σ_b without a target configuration ($\boldsymbol{X}^0 = 0$), and Figure 3.5 pictures the results. As pointed out above, the membrane in this case will reach a circular equilibrium configuration. Just as in case 1, the conservation of area leads the equilibrium radius r_{eq} to be $r_{eq} = 0.2$, because $r_1 = 0.1$ and $r_2 = 0.4$. The equilibrium radius $r_{eq} = 0.2$ is used as a reference to indicate the difference between the computed equilibrium radius and the exact value. Figure 3.5 indicates that the membrane oscillates at a higher frequency as σ_b increases, and it damps out more quickly as well.
We also give the solution profiles at various times for the case $\sigma_b = 300$ in Figure 3.6.

3.3.2 Bending Force With Target Configuration

In this section, we implement a target configuration $\boldsymbol{X}^0$ in the bending force formula, where $\boldsymbol{X}^0$ is defined as

$$\begin{cases} X^0(s) = 0.5 + 0.05 \cdot \cos(2\pi s), \\ Y^0(s) = 0.5 + 0.2 \cdot \sin(2\pi s). \end{cases}$$

We use different values of the semi-major and semi-minor axes for the target shape than for the initial values $r_1 = 0.4, r_2 = 0.1$. The reason for using a smaller target shape than the equilibrium shape is to ensure that there is a non-zero force at the equilibrium state, which helps to keep the dynamics stable.

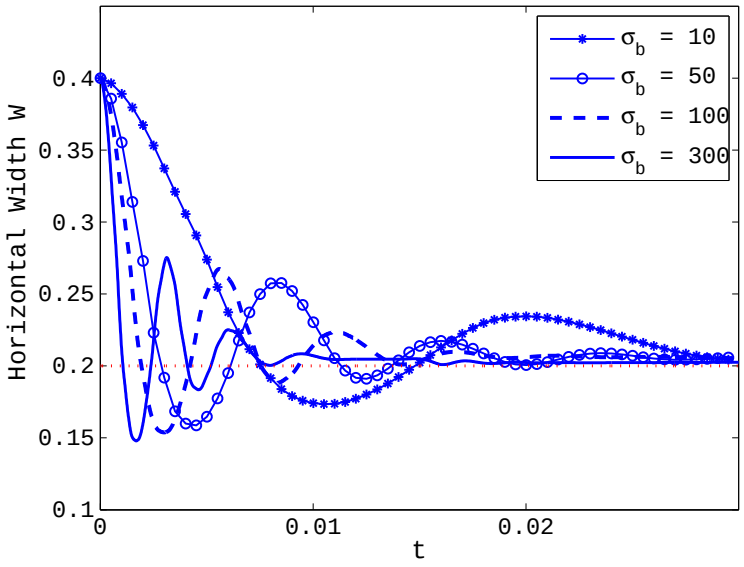

Figure 3.5: Case 2 (bending only): Oscillations with different bending stiffness σ_b.

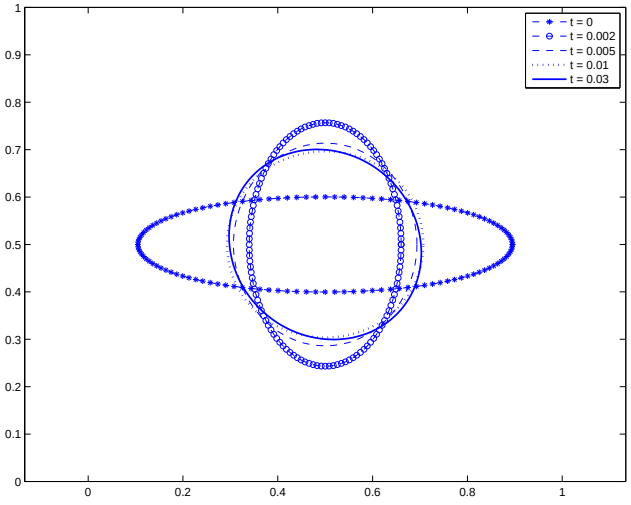

Figure 3.6: Case 2 (bending only): Membrane profiles for bending stiffness $\sigma_b = 300$ and $\boldsymbol{X}^0 = 0$.

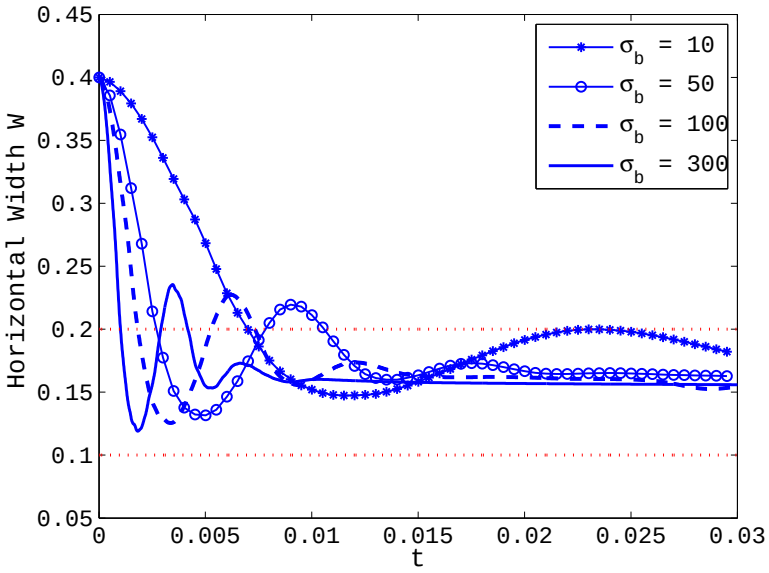

Figure 3.7: Case 2 (bending only): Oscillation with a bending force and elliptical target shape. The horizontal line at $w = 0.1$ aims to show $r_{eq} > 0.1$.

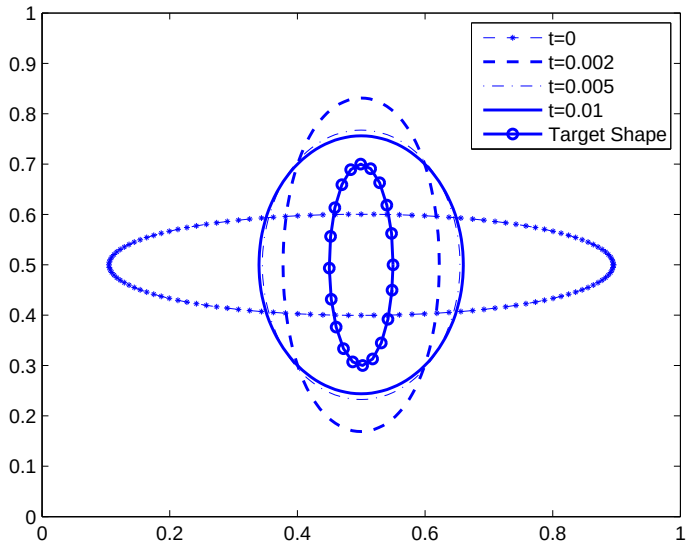

Figure 3.8: Case 2 (bending only): Membrane profiles for bending stiffness $\sigma_b = 300$ and an elliptical target shape.

Different values of bending stiffness σ_b are tested and Figure 3.7 shows that the equilibrium shape is not a circle but is rather an ellipse having semi-axes around $r_1 \approx 0.12$ and $r_2 \approx 0.26$. The non-circular target configuration $\boldsymbol{X}^0$ affects the equilibrium configuration and results in a significant change in the equilibrium shape. Also, the area of the equilibrium configuration $\boldsymbol{X}^0$ is approximately the same as for the initial configuration, due to the conservation of area. The equilibrium configuration in Figure 3.8 is an ellipse with semi-axes in the same direction as the target ellipse, while in Figure 3.6 the equilibrium configuration is a circle with radius $r = 0.2$.

3.4 Case 3: Stretching Force and Bending Force

In this section, we will study the membrane dynamics caused by a combination of stretching and bending forces, and then determine for what values of σ_b and σ_s each force is dominant.

The presence of the fourth-derivative in the bending force implies that it has a more rigid restriction on time step Δt than for the second-derivative formula for stretching force [9]. In order to simplify our parameter study, all of the following simulations fix σ_b and vary σ_s. The choice of σ_b is based on a value that is capable of generating clear oscillations as observed in case 2 but not so large that an extremely small time step is required. We aim to keep the time step above $\Delta t \geq 10^{-6}$, and ideally around $\Delta t \approx 10^{-5}$. The pattern of the oscillations are used as a criteria to determine whether the dominant force is due to stretching or bending. For example, if the membrane oscillations for case 3 are similar to that of case 1, we conclude that the stretching force is the dominant force, otherwise, we conclude that the bending force dominates the oscillation.

As described above, without the equilibrium configuration $\boldsymbol{X}^0$ in the bending force formula, the equilibrium configuration is a circle similar to case 1. From this perspective, we are not able to see any change in the equilibrium shape, thus we are not able to identify which force dominates the equilibrium configuration. In this section, therefore, an elliptical target configuration is included in all simulations, so that the equilibrium configuration is no longer circular.

To ensure that stretching and bending effects are comparable in size, we want the magnitude of the first oscillation driven by the bending force at around the same value as that for the stretching force. Different values of stretching stiffness σ_s and bending stiffness σ_b have already been considered in the previous two sections, with the results summarized in

Figures 3.2 and 3.7. We choose bending stiffness $\sigma_b = 300$ and $\sigma_s = 2000$ as "reference values", because both have an overshoot in the membrane width for the first oscillation around $t \approx 0.1$ and the oscillation frequency is also comparable. This implies that the oscillations caused by these two forces are similar in that the stretching force has a similar effect to the bending force at this particular elastic stiffness value. We define the ratio between the stretching stiffness and bending stiffness, $\lambda = \frac{\sigma_s}{\sigma_b}$, as an indicator for the dominant force measurement and we aim to find an upper bound for λ where the stretching force dominates and a lower bound for λ where the bending force dominates.

First, we try to find the upper bound for λ when bending stiffness is fixed at $\sigma_b = 300$, and stretching stiffness varies. Figure 3.9 shows the case that stretching force dominates the oscillation. The stretching stiffness varies from $\sigma_s = 24000$ through $\sigma_s = 27000, \sigma_s = 30000$ to $\sigma_s = 36000$. We can conclude from the simulations in Figure 3.9, as we proceed from subplots $(a), (b), (c), (d)$:

- Stretching starts to dominate for values of $\sigma_s \gtrapprox 27000$.
- If $\sigma_s \gtrapprox 36000$, the bending effect is no longer visible.
- The stretching force begins to dominate when $\sigma_s/\sigma_b \gtrapprox 36000/300 = 120$.

Secondly, we try to find the lower bound of λ below which bending force dominates. We choose stretching stiffness values from $\sigma_s = 1200, 4800, 7200$, and 9600. We can conclude from the simulations in Figure 3.10 as we proceed through subplots from $(a), (b), (c), (d)$:

- Bending starts to dominate the oscillations for values $\sigma_s \lessapprox 4800$.
- If $\sigma_s \lessapprox 1200$, the stretching effect is no longer visible.
- The range in which stretching force dominates is around $\sigma_s/\sigma_b \lessapprox 1200/300 = 4$.

3.5 Summary

We can reach the following conclusions based on the simulations from all three cases:

- The equilibrium configuration for case 1 (stretching only) is a circle, which has the same area as the initial configuration due to area conservation.
- The equilibrium configuration of case 2 (bending only) is also a circle, if only there is no target shape $\boldsymbol{X}^0$. Simulations with a non-circular target configuration $\boldsymbol{X}^0$ have a different equilibrium configuration.
- For the simulations of case 3 (combining stretching and bending forces), stretching force dominates if $\sigma_s/\sigma_b \gtrapprox 120$, while bending force dominates if $\sigma_s/\sigma_b \lessapprox 4$. If

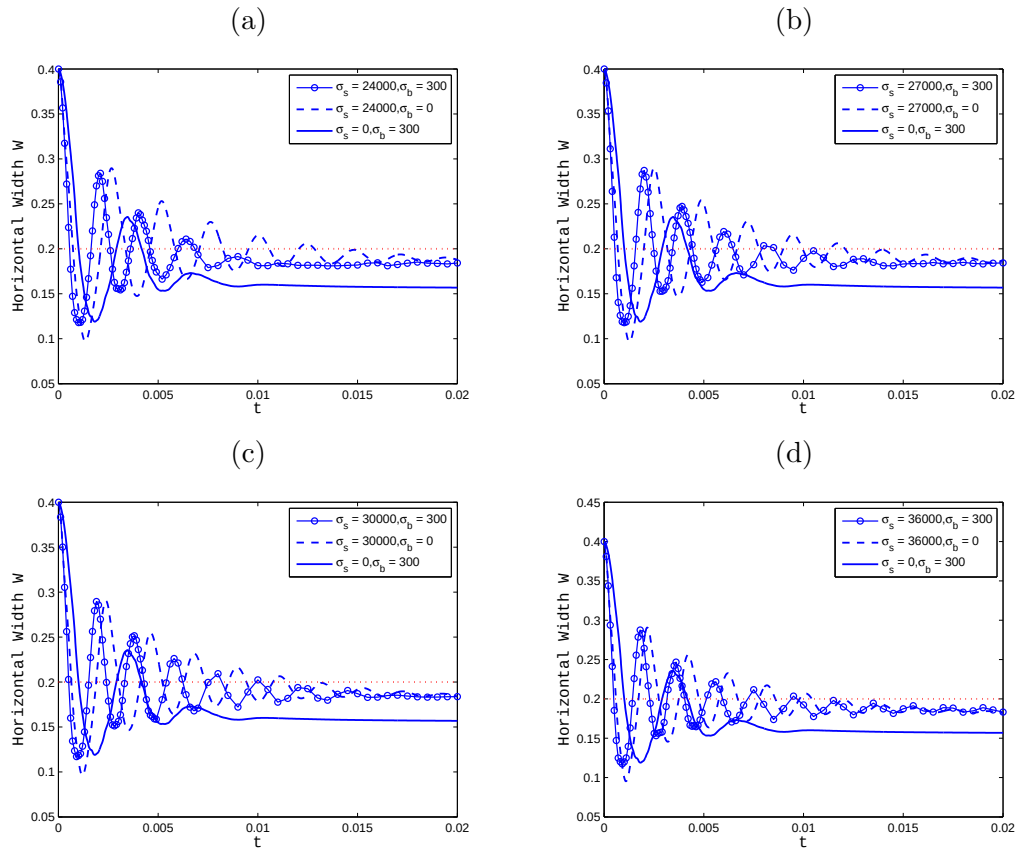

Figure 3.9: Case 3 (bending and stretching): Simulations for the stretching-dominant situation.

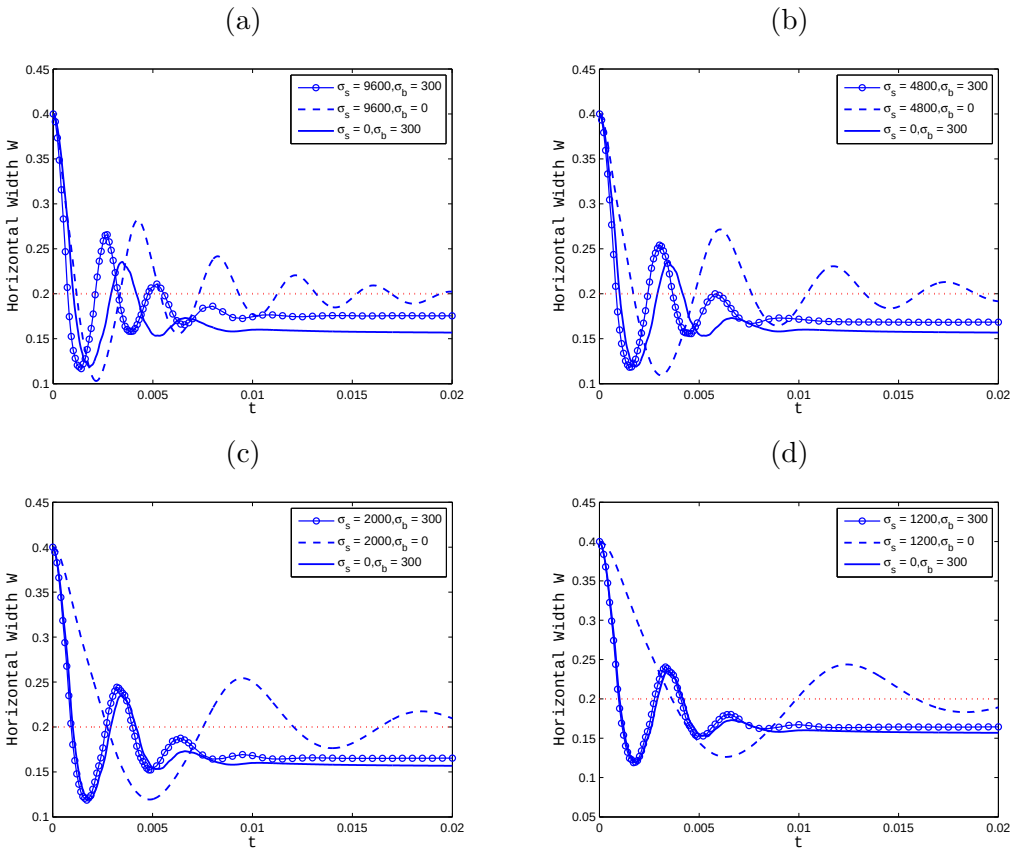

Figure 3.10: Case 3 (bending and stretching): Simulations for the bending-dominant situation.

$4 \lessapprox \sigma_s/\sigma_b \lessapprox 120$, the oscillation is a combination of stretching and bending effects.

- These observations will prove to be helpful when choosing values of the elastic force parameters for our jellyfish simulations in Chapter 4, for which firm estimates of material parameters are not yet available in the literature.

Chapter 4

Two Dimensional Jellyfish Simulations

In this chapter, we apply the IB method described in Chapter 2 to study the motion of an open, elastic membrane immersed in fluid, where the elastic effects are caused by two forces, a stretching force and a bending force. We first introduce the geometry of the open membrane problem and then simulations are performed to illustrate the dynamics of an open membrane that starts from an initial configuration and ends at a preset target configuration under the effects of these two elastic forces. The simulations aim to validate the stretching and bending force calculations, and the geometries of boundary conditions for the membrane. Finally, we extend the open membrane simulation to a two dimensional jellyfish model using parameters extracted from the experiments in [3].

4.1 Simulations of An Open Membrane

In this section, we study an open membrane immersed in a two dimensional fluid domain pictured in Figure 4.1. The fluid domain is defined as $\Omega = [0,1] \times [0,1]$, and the membrane is denoted as Γ. The fluid domain Ω has periodic boundary conditions in both x- and y-directions, and it is defined on an Eulerian grid. The membrane is defined on a Lagrangian grid with a parameterization of $s \in [0,1]$, and the membrane points are equally spaced in s along Γ with a grid spacing of Δs. The initial configuration of Γ is defined by the following equation:

$$\begin{cases} X^{(1)}(s) = x_0 + r_1 \cdot \cos(\pi s), \\ Y^{(1)}(s) = y_0 + r_2 \cdot \sin(\pi s), \end{cases}$$

where $\boldsymbol{X}^{(1)}(s) = (X^{(1)}(s), Y^{(1)}(s))$ represents the initial fibre coordinates, and (x_0, y_0) is the center of the initial configuration. If $r_1 = r_2$, then the initial configuration is a half circle, otherwise it is a half ellipse. The open membrane is elastic and non-porous as stated in Chapter 3. We first point out the main differences between a closed and an open membrane:

- For a closed membrane, there is no boundary condition to apply at the membrane end-points, while for an open membrane, we need to specify the boundary conditions at each end.
- For the open membrane, area conservation does not hold anymore.
- In the open case, the membrane eventually settles down to the resting state defined by the target configuration $\boldsymbol{X}^0$ in Equation (2.14) and has the resting length R in Equation (2.11). This is in contrast to the closed case where the steady state configuration need not coincide with the target if the membrane is pressurized.

4.1.1 Boundary Condition of the Open Membrane

An open membrane moves freely within the fluid and so the end-points can be assumed to obey end-point conditions commonly applied to other similar structures such as cantilever beams [15]. In particular, we impose the boundary conditions

$$\frac{\partial^2 \boldsymbol{X}}{\partial s^2} = 0, \tag{4.1}$$

$$\frac{\partial^3 \boldsymbol{X}}{\partial s^3} = 0, \tag{4.2}$$

at the end-points $s = 0$ and $s = 1$. Equation (4.1) indicates that the curvature at the two free ends is zero, and Equation (4.2) indicates that the rate of change of curvature is also zero; in other words, the ends are treated as "free ends" at which the membrane is as flat as possible. In order to approximate the second and third derivatives of $\boldsymbol{X}$, two fictitious points are introduced at each end, and Figure 4.2 illustrates the location of these fictitious

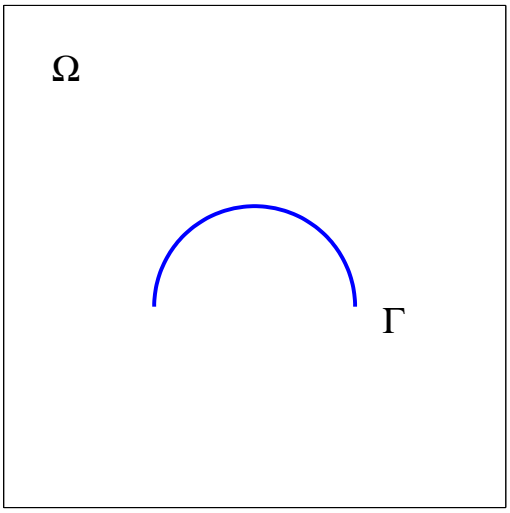

Figure 4.1: An open membrane Γ immersed in the fluid domain Ω.

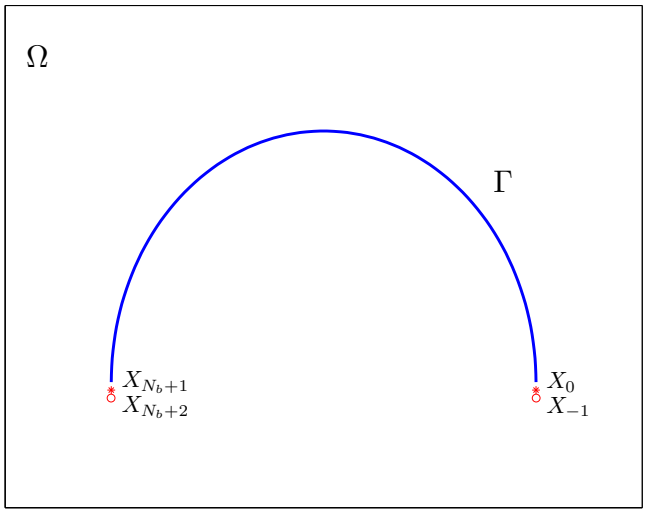

Figure 4.2: Open membrane with fictitious points.

points. The Lagrangian parameterization $s \in [0,1]$ is defined to be counter-clockwise along the membrane, so that $\boldsymbol{X}_0$ and $\boldsymbol{X}_{-1}$ are the two fictitious points associated with $s = 0$, while $\boldsymbol{X}_{N_b+1}$ and $\boldsymbol{X}_{N_b+2}$ are associated with $s = 1$.

We can then derive by Taylor series the discrete approximations for the boundary conditions. Given formulas for $\boldsymbol{X}_{ss} = 0$ and $\boldsymbol{X}_{sss} = 0$ at $s = 0$, we have,

$$\begin{cases} \boldsymbol{X}_{ss}|_{s=0} \approx \frac{\boldsymbol{X}_0 - 2\boldsymbol{X}_1 + \boldsymbol{X}_2}{\Delta s^2} = 0, \\ \boldsymbol{X}_{sss}|_{s=0} \approx \frac{\boldsymbol{X}_2 - 3\boldsymbol{X}_1 + 3\boldsymbol{X}_0 - \boldsymbol{X}_{-1}}{\Delta s^3} = 0, \end{cases}$$

These equations can be solved to obtain the following values for the fictitious points at $s = 0$:

$$\begin{cases} \boldsymbol{X}_0 = 2\boldsymbol{X}_1 - \boldsymbol{X}_2, \\ \boldsymbol{X}_{-1} = 3\boldsymbol{X}_1 - 2\boldsymbol{X}_2, \end{cases}$$

with similar equations at $s = 1$:

$$\begin{cases} \boldsymbol{X}_{N_b+1} = 2\boldsymbol{X}_{N_b} - \boldsymbol{X}_{N_b-1}, \\ \boldsymbol{X}_{N_b+2} = 3\boldsymbol{X}_{N_b} - 2\boldsymbol{X}_{N_b-1}, \end{cases}$$

where $\boldsymbol{X}_1, \boldsymbol{X}_2, \boldsymbol{X}_{N_b-1}, \boldsymbol{X}_{N_b}$ are interior or real membrane points. The above formulas are used to replace the fictitious point values wherever they appear in the discrete equations described in Chapter 3.

We note that our jellyfish model can be extended to three dimensions by treating the bell as a two dimensional surface consisting of an interwoven network of two types of fibers as pictured in Figure 4.3: one set of fibers that winds around the bell tangentially to the bell edge, and a second set that runs normal to the edge and intersect at the bell apex. The tangential fibers are closed loops that obey a periodic boundary condition in s. The normal fibers on the other hand are open fibers that are similar to those used in our two dimensional model, where we applied open end-point boundary conditions.

4.1.2 Open Membrane with Target Configuration

In order to verify the effects of the resting length R in Equation (2.11) and the effects of the target configuration $\boldsymbol{X}^0$ in Equation (2.14) separately, we set up two test simulations

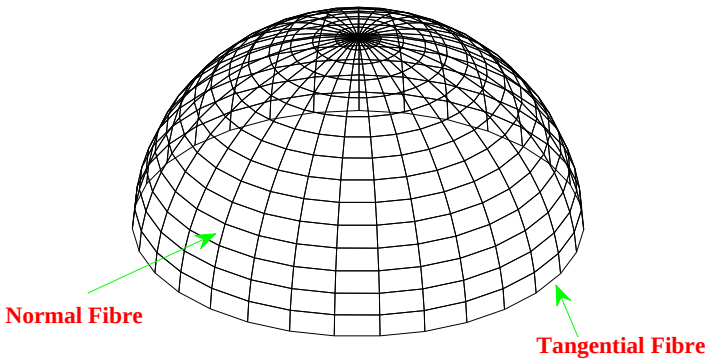

Figure 4.3: Three dimensional model.

and use the same elastic parameters, $\sigma_s = 30000$ and $\sigma_b = 1000$. In these two simulations, the membrane has the same initial configuration, which is defined by

$$\begin{cases} X^{(1)}(s) = 0.5 + 0.1297 \cdot \cos(\pi s), \\ Y^{(1)}(s) = 0.5 + 0.2594 \cdot \sin(\pi s), \end{cases}$$

but different target configuration, which are pictured in Figure 4.4. The fluid parameters are the same as those used in Chapter 3. By taking a given resting length R calculated from the initial configuration and a large stretching stiffness σ_s, the membrane length is kept approximately constant. In this way, we can focus on the bending dynamics in the simulation, which is important in the jellyfish simulations in the next section.

In our first test, the membrane is left to evolve from an elliptical initial configuration to a flat line, and the resting length is set equal to the total length of the initial configuration, $R = 0.6283$. The equation of the target configuration is:

$$\begin{cases} X^{(2)}(s) = 0.5 + (s - 0.5) \cdot R, \\ Y^{(2)}(s) = 0.5. \end{cases}$$

Different values of σ_s and σ_b are tested and Figure 4.5 pictures the profile of the membrane as

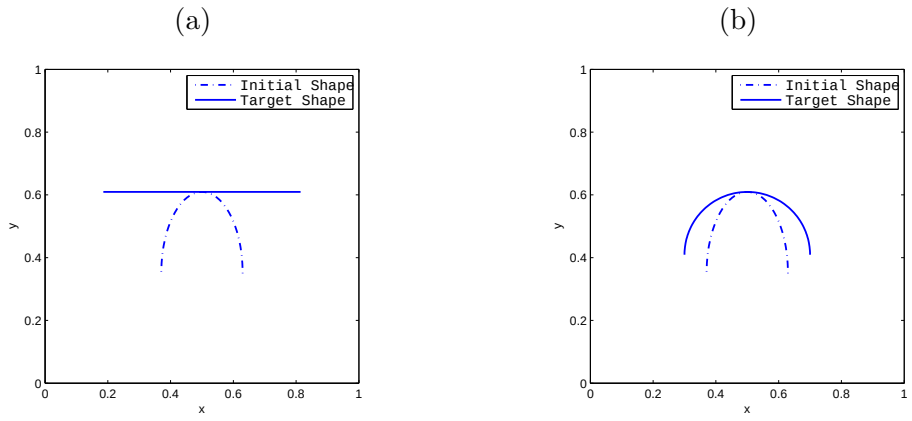

Figure 4.4: (a) First "flat membrane" test.(b) Second "curved membrane" test.

it progresses from an elliptical initial configuration to a flat configuration. Figure 4.6 shows the time variation of the membrane length. These two figures indicate that the membrane profile oscillates and settles down to the target flat line. The length of the membrane also oscillates and the change in length is within roughly 15% of the target length. Note that the length could be constrained more tightly by choosing a larger value of σ_s, but then this would require a smaller time step.

In our second test, the membrane evolves from its initial elliptical configuration to a half-circle with the same length, corresponding to the target configuration

$$\begin{cases} X^{(2)}(s) = 0.5 + 0.2 \cdot \cos(\pi s), \\ Y^{(2)}(s) = 0.5 + 0.2 \cdot \sin(\pi s). \end{cases}$$

Several snapshots of the evolving membrane are shown in Figure 4.7. The elastic forces clearly drive the membrane to move towards the target configuration. Furthermore, as the membrane moves from its initial configuration to the target configuration, it actually begins to shift down slightly toward the $x-$axis. This is because the membrane initially pushes the neighboring fluid upward as it is opening, and the resulting flow in return forces the membrane to move downward. Figure 4.8 shows that the membrane length also settles down after a short period of oscillation, and the bell length remains within roughly 10% of the target length for the entire simulation, which is a significant improvement over the first "flat membrane" test. This is not surprising since the initial and target configurations are much closer which mean that the forces driving the curved membrane are much smaller.

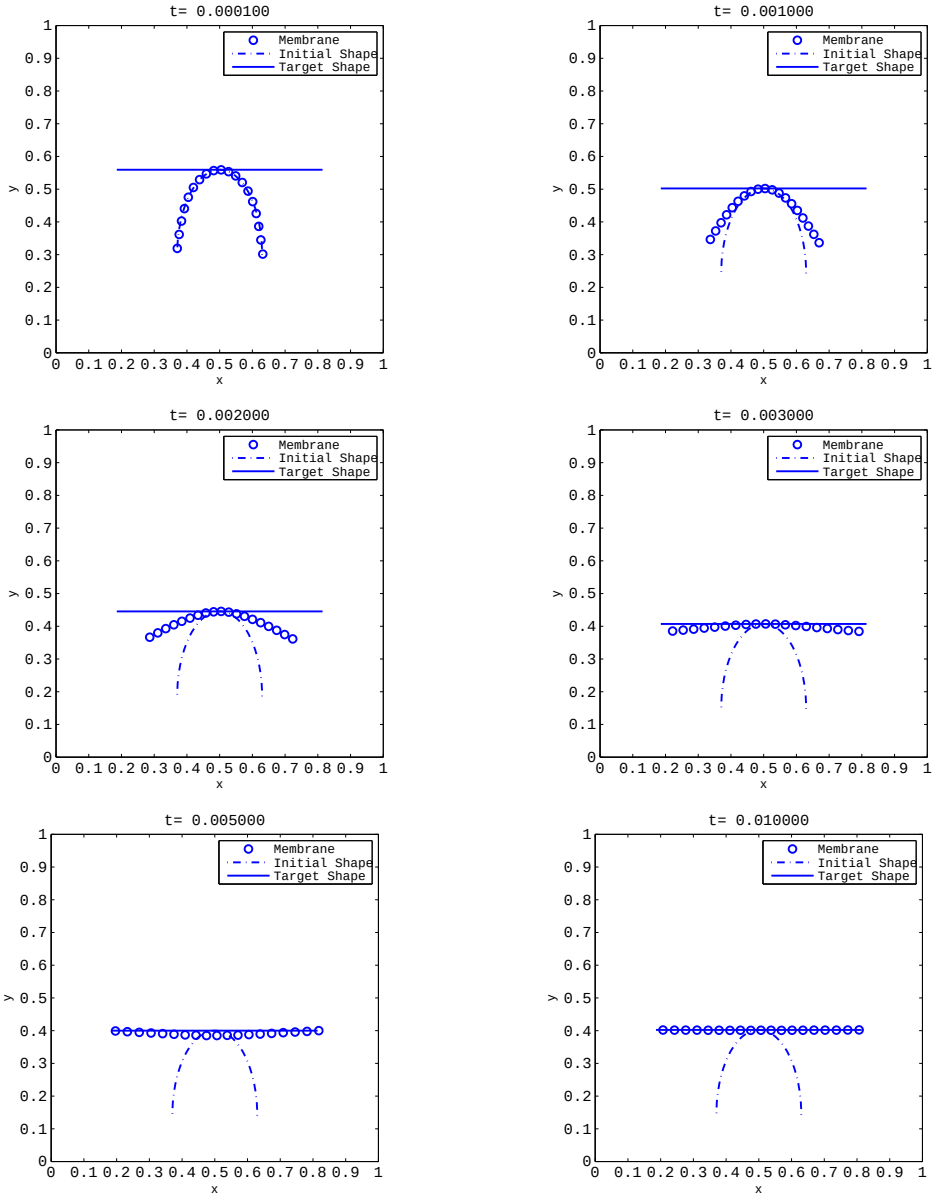

Figure 4.5: Time evolution of the membrane in the first "flat membrane" test.

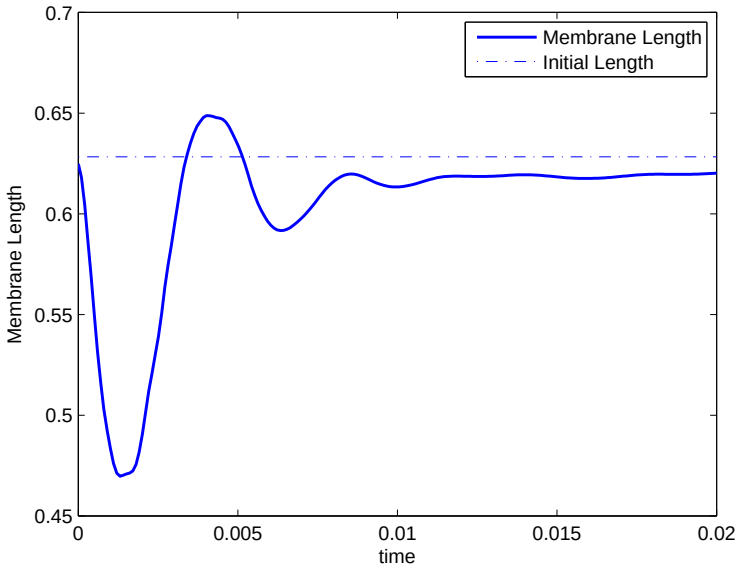

Figure 4.6: Length oscillation in the first "flat membrane" test.

4.2 Non-Dimensionalization of the IB Model

The fluid solver we are using is restricted to computing on a fluid domain of size 1×1. In order to simulate a jellyfish of arbitrary size, we can either scale our simulation so that the Reynolds number Re is comparable between the experiments and simulations, or modify the code to deal with domains of arbitrary size. We have chosen the former approach, treating the domain to be of size $1cm \times 1cm$, and choosing parameters in our simulations (ρ, μ), so that the Reynolds number matches that of the corresponding experiments. We define dimensionless parameters, choosing $\tilde{x} = \frac{x}{L}$, where L is the radius of the bell, $\tilde{t} = t \cdot \omega$, where ω is the swimming frequency with unit of s^{-1}, and the dimensionless velocity is $\tilde{u} = \frac{u}{\omega L}$.

The dimensionless Navier-Stokes equations are

$$\begin{aligned} \tilde{\boldsymbol{U}}_{\tilde{t}} + \tilde{\boldsymbol{U}} \cdot \tilde{\nabla} \tilde{\boldsymbol{U}} &= \frac{\mu}{\rho \omega L^2} \tilde{\Delta} \tilde{\boldsymbol{U}} - \frac{1}{\rho \omega^2 L^2} \tilde{\nabla} P + \frac{1}{\rho \omega^2 L} \boldsymbol{f}, \\ \tilde{\nabla} \cdot \tilde{\boldsymbol{U}} &= 0. \end{aligned} \tag{4.3}$$

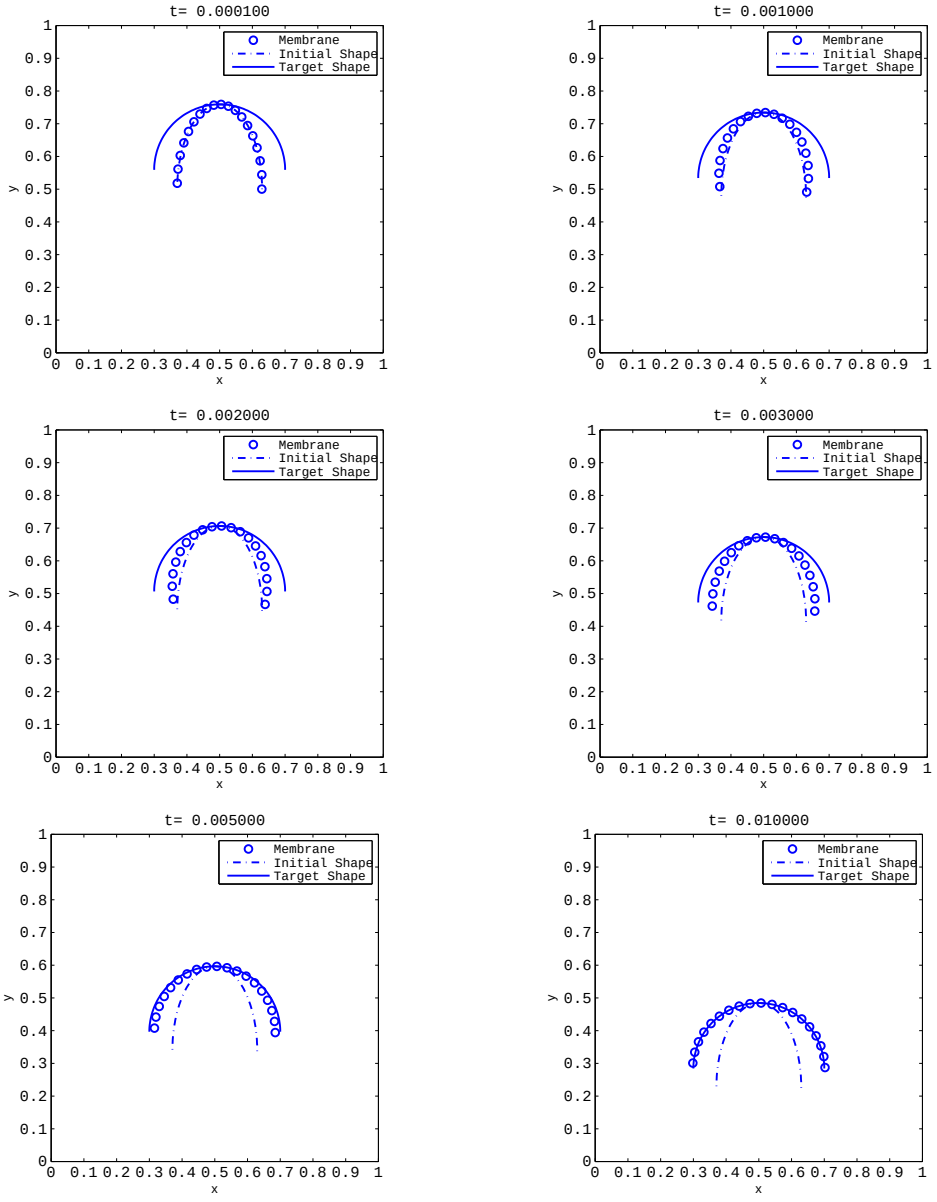

Figure 4.7: Time evolution of the membrane in the second "curved membrane" test.

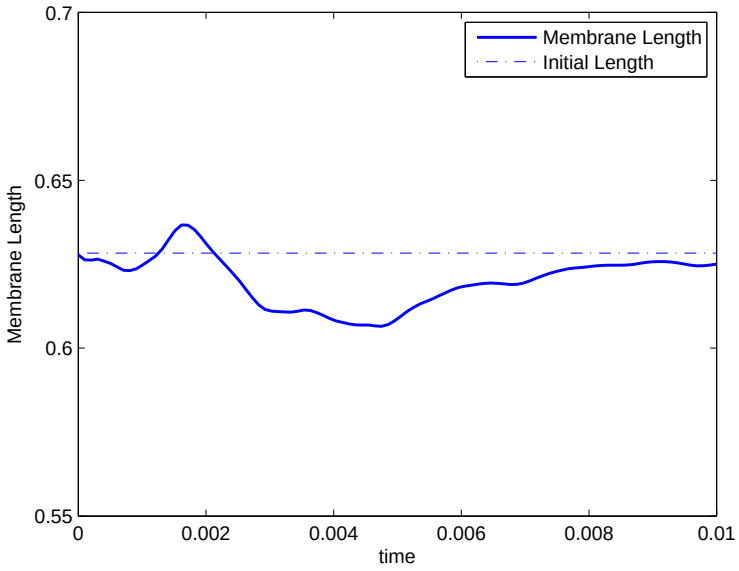

Figure 4.8: Length oscillation in the second "curved membrane" test.

We then define

$$\begin{aligned} Re &= \frac{\rho\omega L^2}{\mu}, \\ \tilde{P} &= \frac{P}{\rho\omega^2 L^2}, \\ \tilde{\sigma_s} &= \frac{\sigma_s}{\rho\omega^2 L^2}, \\ \tilde{\sigma_b} &= \frac{\sigma_b}{\rho\omega^2 L^2}, \end{aligned} \tag{4.4}$$

after which Equation (4.3) can be written as

$$\begin{aligned} \tilde{\boldsymbol{U}}_{\tilde{t}} + \tilde{\boldsymbol{U}} \cdot \tilde{\nabla}\tilde{\boldsymbol{U}} &= \frac{1}{Re}\tilde{\Delta}\tilde{\boldsymbol{U}} - \tilde{\nabla}\tilde{P} + \tilde{\boldsymbol{f}}, \\ \tilde{\nabla} \cdot \tilde{\boldsymbol{U}} &= 0, \end{aligned} \tag{4.5}$$

where the dimensionless force density is

$$\tilde{\boldsymbol{f}} = \int_\Gamma \left[\tilde{\sigma}_s \frac{\partial}{\partial s} \left(\frac{\partial \tilde{\boldsymbol{X}}}{\partial s} \left(1 - \frac{\tilde{R}}{|\frac{\partial \tilde{\boldsymbol{X}}}{\partial s}|} \right) \right) + \tilde{\sigma}_b \left(\frac{\partial^4 \tilde{\boldsymbol{X}^{(2)}}}{\partial s^4} - \frac{\partial^4 \tilde{\boldsymbol{X}}}{\partial s^4} \right) \right] \delta(\boldsymbol{x} - \boldsymbol{X}) ds. \tag{4.6}$$

For the two dimensional jellyfish model described in the next section, we focus on solving the dimensionless Navier-Stokes equations (4.6), and compare the emergent swimming

dynamics with corresponding experimental results. The experimental data are converted to dimensionless values, as are the results for the IB model. We keep the dimensionless time parameter $\tilde{t} = 1$ the same and compare the results of the simulations and experiments in dimensionless form.

4.3 Simulation of a Swimming Jellyfish

The swimming motion of a real jellyfish is driven by the periodic contraction of the jellyfish bell, in which bioelectricity passes through the body and activates muscle contractions. The magnitude of the contraction force is governed by neural and motion feed back [7]. Research on the hydrodynamic swimming performance of jellyfish includes both experimental and analytical studies [3, 6, 17, 18].

4.3.1 Two Dimensional IB Jellyfish Model

In this section, we propose to study the swimming motion of jellyfish using a two dimensional IB model. The motion of the jellyfish in our model is driven solely by the fluid-structure interaction between the elastic (stretching and bending) membrane forces and the fluid, which is different from the model proposed by Miller [13], where bell location obtained by motion capture are imposed. One major limitation of our two dimensional jellyfish model is that our two dimensional bell corresponds in three dimension to a curved sheet of infinite extent and not a round hemispherical bell. We aim to use this simple two dimensional open membrane to capture some essential characteristics of the jellyfish swimming motion. The membrane is also referred as the jellyfish bell, and so in this section, we use the terms membrane and bell interchangeably.

To mimic the contraction force that drives the motion, we use a horizontal spring force at each end point of the bell to simulate the muscle contraction. A representative bell shape and contraction force are pictured in Figure 4.9.

In order to set up a jellyfish model with realistic physical and geometric properties, we use the experimental data from [3]. Figure 4.10 reproduces Figure 3 from [3] that show the swimming dynamics of various species of jellyfish in terms of time dependent plots of aspect ratio, position, velocity and Reynolds number. The initial and target configurations of the bell in our simulations are chosen based on the aspect ratio of the bell (the "F_i" value in Table 4.1). A diagram depicting the initial and target configurations is given in Figure

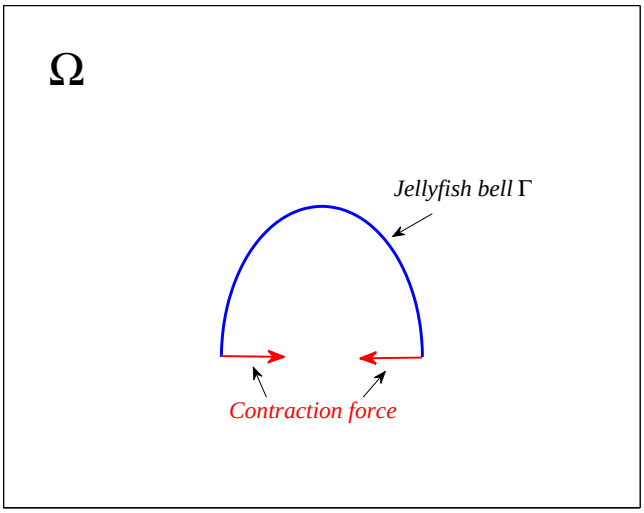

Figure 4.9: General representation of the two dimensional IB bell model, with contraction force.

4.11. The most contracted configuration corresponds to that with maximum aspect ratio and is referred to as configuration 1 (which is also used as the initial state); the most open configuration with minimum aspect ratio is referred to as configuration 2.

The swimming motion of a jellyfish can be divided into two phases, which we referred to as the "recovery phase" and the "contraction phase". In the recovery phase, the bell opens from configuration 1 to configuration 2 under the effects of the bending force, while the contraction force is inactive. In the contraction phase, the bell moves from configuration 2, the initial configuration in this phase, to configuration 1 under the action of the contraction force. The stretching and bending forces are also active during this time. Configuration 2 is not only the initial configuration in the contraction phase, but also the target configuration in the recovery phase. The contraction force is varied periodically so that one full swimming period contains one contraction phase and one recovery phase. The bell moves between the two configurations as pictured in Figure 4.11. The time spent in a full swimming period is referred as T_s, the time spent in the contracting phase is t_{close}, and the time spent in the recovery phase is t_{open}, so that $T_s = t_{close} + t_{open}$.

In order that bell movements are easily observed, we choose a jellyfish species for

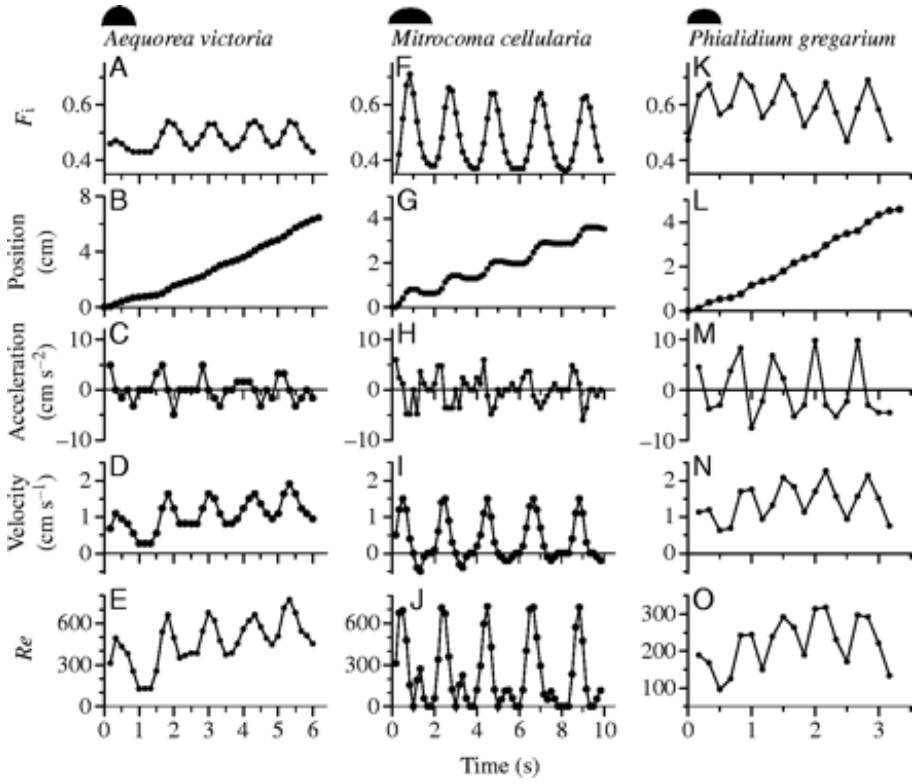

Figure 4.10: Experimental data for six species of jellyfish. Reprinted with permission of the *Journal of Experimental Biology* [3, Figs. 3].

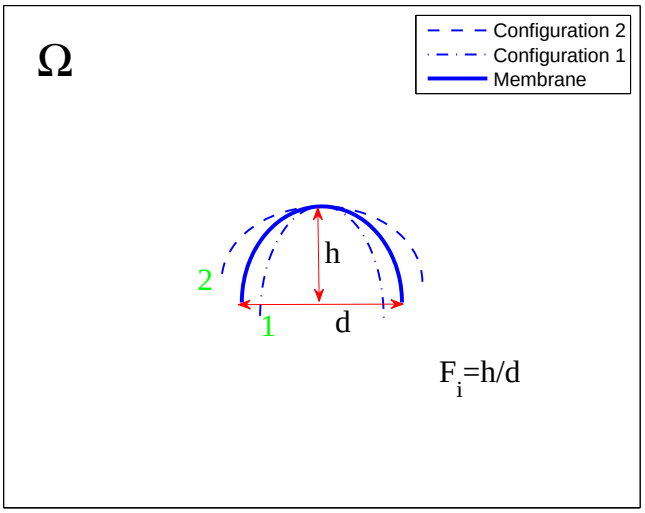

Figure 4.11: Configuration 1 (relaxed, minimum F_i) and configuration 2 (contracted, maximum F_i) in one swimming period.

which the difference between configurations 1 and 2 is large enough to generate a significant bending force. After comparing the six species of jellyfish in [3], we chose to simulate *Mitrocoma cellularia* as our "base case". Then we use the same material properties (bending and stretching stiffness) and contraction force to simulate a second species (*Aequorea victoria*) but change the frequency of the contraction force and aspect ratio according to experimental data in Figure 4.10. We make the following assumptions in both cases:

- Jellyfish of comparable size generate comparable contraction force.
- Jellyfish of comparable size have comparable material properties (bending and stretching stiffness).
- Swimming dynamics are dependent on the bell size and the contraction force.

The material parameters for the bell (stretching stiffness σ_s and bending stiffness σ_b) and the amplitude of contraction force f_c are estimated using the following procedure:

- Stretching stiffness σ_s: in experiments, the length of the bell does not change significantly, and so we simply choose the stretching stiffness σ_s to be large enough that the bell keeps within 10%–15% of its initial/resting length throughout the simulation.

- Bending stiffness σ_b: the value of σ_b is chosen such that the time for the bell to open from configuration 1 to configuration 2 is similar to that of the experimental results. This assumes that between configuration 1 and configuration 2, the contraction force is off and the elastic force of the bell is active.
- Contraction force $f_c(t)$: the magnitude of f_c is chosen so that the time for the bell to contract from configuration 2 to configuration 1 is the same as that in experiments. The frequency (on/off) character of the contraction is estimated directly from the data in Figure 4.10. More details about defining the parameters are provided in the following sections.

Our two dimensional IB model is based on [3] and aims to simulate the swimming motion of jellyfish, and capture realistic swimming dynamics using the dimensionless form of Navier-Stokes equations, our model is able to simulate jellyfish of arbitrary size. The procedure for comparing experimental data and simulation results is as follows:

1. Convert the experimental data into dimensionless form.
2. Choose parameters for the simulation (based on domain size of $1cm \times 1cm$) so that the Reynolds number Re is the same as in experiments.
3. Convert the simulation results into dimensionless form.
4. Compare the dimensionless results between the experiment and simulation.

For convenience, we have summarized all experimental data and simulation parameters in Table 4.1 in dimensional and dimensionless form (where appropriate). The Reynolds number is calculated according to the definition in Equation (4.4), and the fluid parameters ρ and μ are chosen in order to achieve a balance between a clear bell movement and the computation cost. The bell diameter, aspect ratio, frequency, swimming period, recovery phase and displacement per period are estimated from the experimental data and material properties are chosen from a series of test simulations. The total displacement and average velocity are the values that we focus on for validating our model results.

4.3.2 Jellyfish Model Parameters

The fluid solver computes on a domain $\Omega = [0, 1] \times [0, 1]$ and we choose a bell size $L = 0.1$ that is small enough to minimize the effects of the periodic boundaries. After considering the aspect ratio data from experiments, we set up configuration 2 for *Mitrocoma cellularia*

Table 4.1: Experimental data from [3], and parameters used in the simulations. Dimensional and/or dimensionless values of parameters are shown, where appropriate. The highlighted dimensionless numbers are the prime focus in our comparisons between model and experiments.

Parameter	*Mitrocoma cellularia*				*Aequorea victoria*			
	Experiments		Simulations		Experiments		Simulations	
	(CGS)	(dim'less)	(CGS)	(dim'less)	(CGS)	(dim'less)	(CGS)	(dim'less)
Aspect ratio (F_i)		0.4–0.65		0.45–0.65		0.4–0.55		0.45–0.65
Reynolds number (Re)		200		200		400		400
Fluid density (ρ)	1.0		20		1.0		20	
Dynamic viscosity (μ)	0.01		0.33		0.01		0.33	
Diameter (L)	2.0		0.1		2.0		0.1	
Frequency (ω)	0.5		333		1.0		667	
Swimming period (T_s)	2.0		0.003		1.0		0.0015	
Recovery phase (t_{open})	1.0		0.0015		0.5		0.00075	
Contraction phase (t_{close})	1.0		0.0015		0.5		0.00075	
Stretching stiffness (σ_s)			1.4×10^6				1.4×10^6	
Bending stiffness (σ_b)			1.4×10^5				1.4×10^5	
Contraction stiffness (σ_c)			1.0×10^7				1.0×10^7	
Displacement per period	1–2	0.5–1			1–1.5	0.5–0.75		
Total displacement	3-6	1.5–3	0.3336	3.336	4.5–6	2.25–3	0.2959	2.9585
Average Velocity	0.5–1	0.5–1	37.033	1.111	1.5–2	0.75–1	32.833	0.985

as follows:

$$\begin{cases} X^{m(2)}(s) = 0.5 + 0.1 \cdot \cos(\pi s), \\ Y^{m(2)}(s) = 0.3 + 0.08 \cdot \sin(\pi s), \end{cases}$$

The corresponding configuration 1 (minimum aspect ratio) is defined as follows:

$$\begin{cases} X^{m(1)}(s) = 0.5 + 0.0747 \cdot \cos(\pi s), \\ Y^{m(1)}(s) = 0.3 + 0.1046 \cdot \sin(\pi s). \end{cases}$$

The diameter and minimum aspect ratio of the two species *Mitrocoma cellularia* and *Aequorea victoria* are close enough to each other that configuration 2 for the latter is also defined as:

$$\begin{cases} X^{a(2)}(s) = 0.5 + 0.1 \cdot \cos(\pi s), \\ Y^{a(2)}(s) = 0.3 + 0.08 \cdot \sin(\pi s). \end{cases}$$

The configuration 1 of *Aequorea victoria* is defined as follows:

$$\begin{cases} X^{a(1)}(s) = 0.5 + 0.0819 \cdot \cos(\pi s), \\ Y^{a(1)}(s) = 0.3 + 0.0983 \cdot \sin(\pi s). \end{cases}$$

From the equations, we can tell that *Mitrocoma cellularia* has a slightly wider shape than *Aequorea victoria*.

In our IB model, we choose the fluid density ρ, and the dynamic viscosity μ as listed in Table 4.1. This ensures that the Reynolds number is comparable between experiments and simulations. Furthermore, the choice of frequency and dynamic viscosity also balances the time period of swimming motion and efficiency in the computation.

4.3.3 Stretching and Bending Stiffness for *Mitrocoma cellularia*

Stretching and bending forces are active throughout the simulations. We choose the stretching stiffness constant σ_s to be large enough that it is able to resist a significant change in the bell length; specifically, we aim to keep difference between the maximum and minimum bell length within 10%–15% of its initial value throughout the simulation. The bending force drives the bell to move from configuration 1 to configuration 2 in the recovery phase over a given time period (t_{open}) indicated in Table 4.1.

A series of simulations are performed, and we tested several values of σ_s and σ_b. After comparing the results, we chose $\sigma_s = 1.4 \times 10^6$ and $\sigma_b = 1.4 \times 10^5$ as the material parameters

so as to satisfy the requirements stated above in Section 4.3.1. The resulting time variations of bell length and aspect ratio are shown in Figure 4.12. During the recovery phase, the change in bell length is less than 3% of its resting length in one period, and bell aspect ratio oscillates close to 0.5 after reaching it target configuration 2.

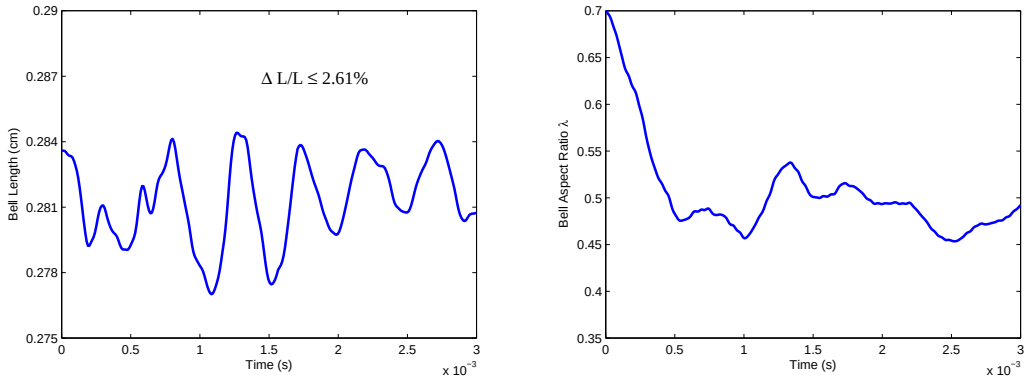

Figure 4.12: Bell length and aspect ratio in the IB model with $\sigma_s = 1.4 \times 10^6$ and $\sigma_b = 1.4 \times 10^5$.

4.3.4 Contraction Force for *Mitrocoma cellularia*

The contraction force is the driving force for the swimming motion, and it arises from a periodic contraction of the bell muscles. In this simulation, we use a time dependent force along the $x-$direction that joins the end points of the bell as pictured in Figure 4.9. The periodicity of the force is based on the time parameters in Table 4.1, in which the force is turned on in the contraction phase for a period of $t_{close} = 0.0015$ and is off in the recovery phase for a period of $t_{open} = 0.0015$. We use a continuous forcing function that has a sinusoidal shape in the contraction phase and equals zero in the recovery phase (see Figure 4.13).

We also define a constant σ_c that represents the magnitude of the contraction force, which we treat as a linear spring having stiffness parameter σ_c. The contraction force is then defined as the product of the contraction stiffness, a periodic forcing factor $k(t)$ and the distance between the current location of the bell end-points and its target location in configuration 1

$$f_c = k(t) \cdot \sigma_c \cdot (d - d_0),$$

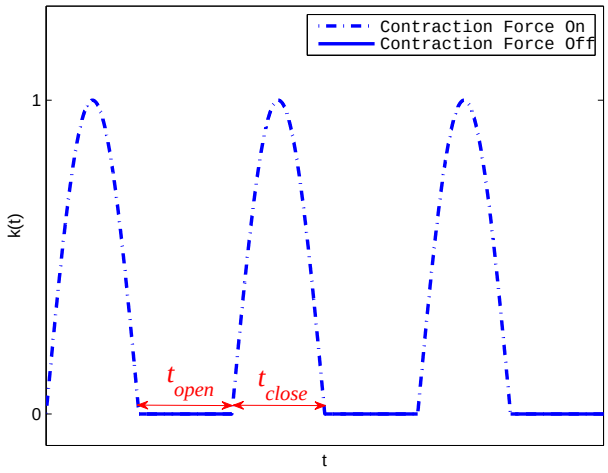

Figure 4.13: Contraction forcing factor $k(t)$.

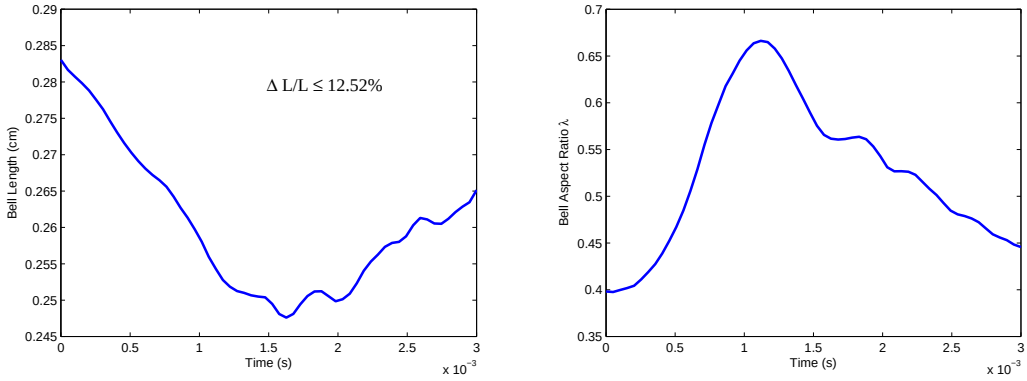

Figure 4.14: Bell length and aspect ratio in the IB model ($\sigma_s = 1.4 \times 10^6$,$\sigma_b = 1.4 \times 10^5$ and $\sigma_c = 1.0 \times 10^7$).

where $d = |\boldsymbol{X}_{N_b} - \boldsymbol{X}_1|$ is the horizontal distance between two end points in the current configuration, and $d_0 = |\boldsymbol{X}^{(1)}_{N_b} - \boldsymbol{X}^{(1)}_1|$ is the horizontal distance between two end points at configuration 1.

We tested several σ_c values and compared the results, and we choose $\sigma_c = 10^7$ following the requirements in Section 4.3.1. The length and aspect ratio of the bell in one complete period are pictured in Figure 4.14. The length of the bell shrinks slightly during the contraction phase, which is due to compression from the tangential component of the contraction force, and the length ultimately decreases by 12% of the resting length. The bell aspect ratio varies between 0.4 and 0.65 which is expected range for *Mitrocoma cellularia* in Figure 4.10.

4.3.5 Simulations of *Mitrocoma cellularia*

We next compare certain features of the simulated swimming motion, such as displacement, average velocity and bell aspect ratio over a several periods of the swimming motion. We then transfer the simulated and experimental results into dimensionless values as described above, at which point we can directly compare the results.

In order to demonstrate that the simulations yield a stable swimming motion of the jellyfish, we simulate for three complete swimming periods. The length of the bell and the aspect ratio in the three periods are shown in Figure 4.15. The corresponding bell displacement and velocity are pictured in Figure 4.16 and Figure 4.17. Figure 4.18 also contains several snapshots of the swimming dynamics at various times.

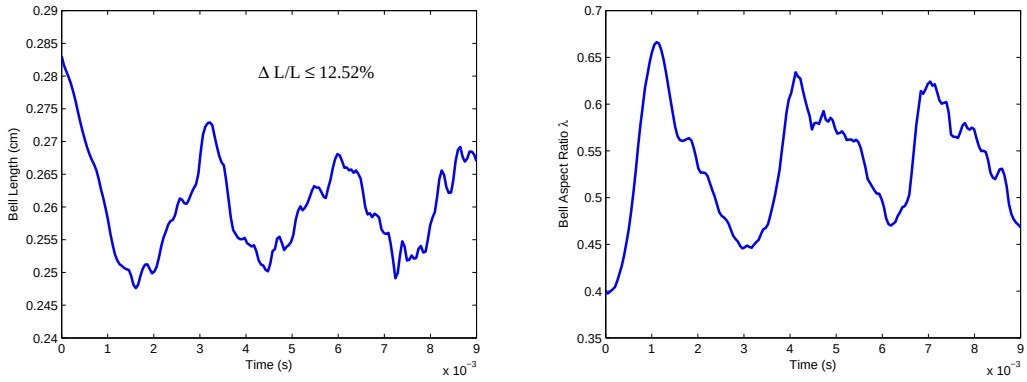

Figure 4.15: Bell length and aspect ratio for *Mitrocoma cellularia*.

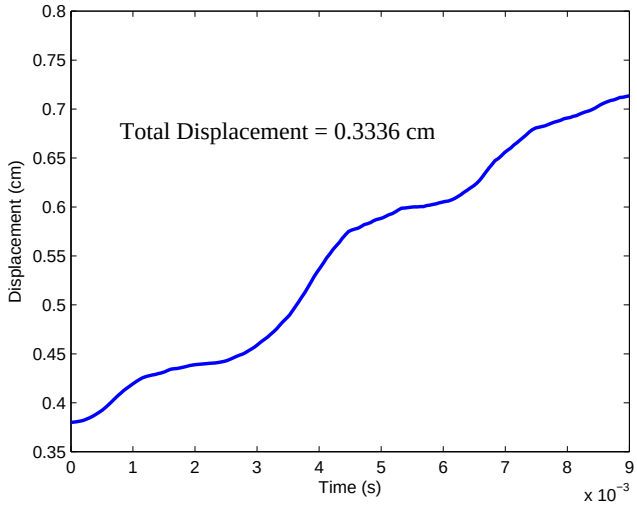

Figure 4.16: Displacement for *Mitrocoma cellularia*.

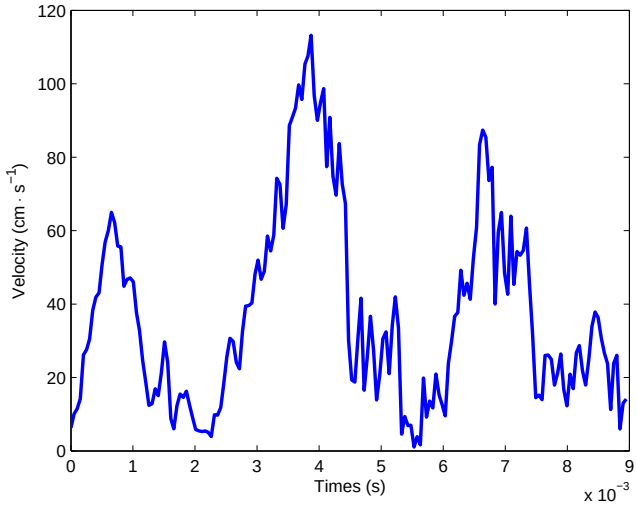

Figure 4.17: Velocity for *Mitrocoma cellularia*.

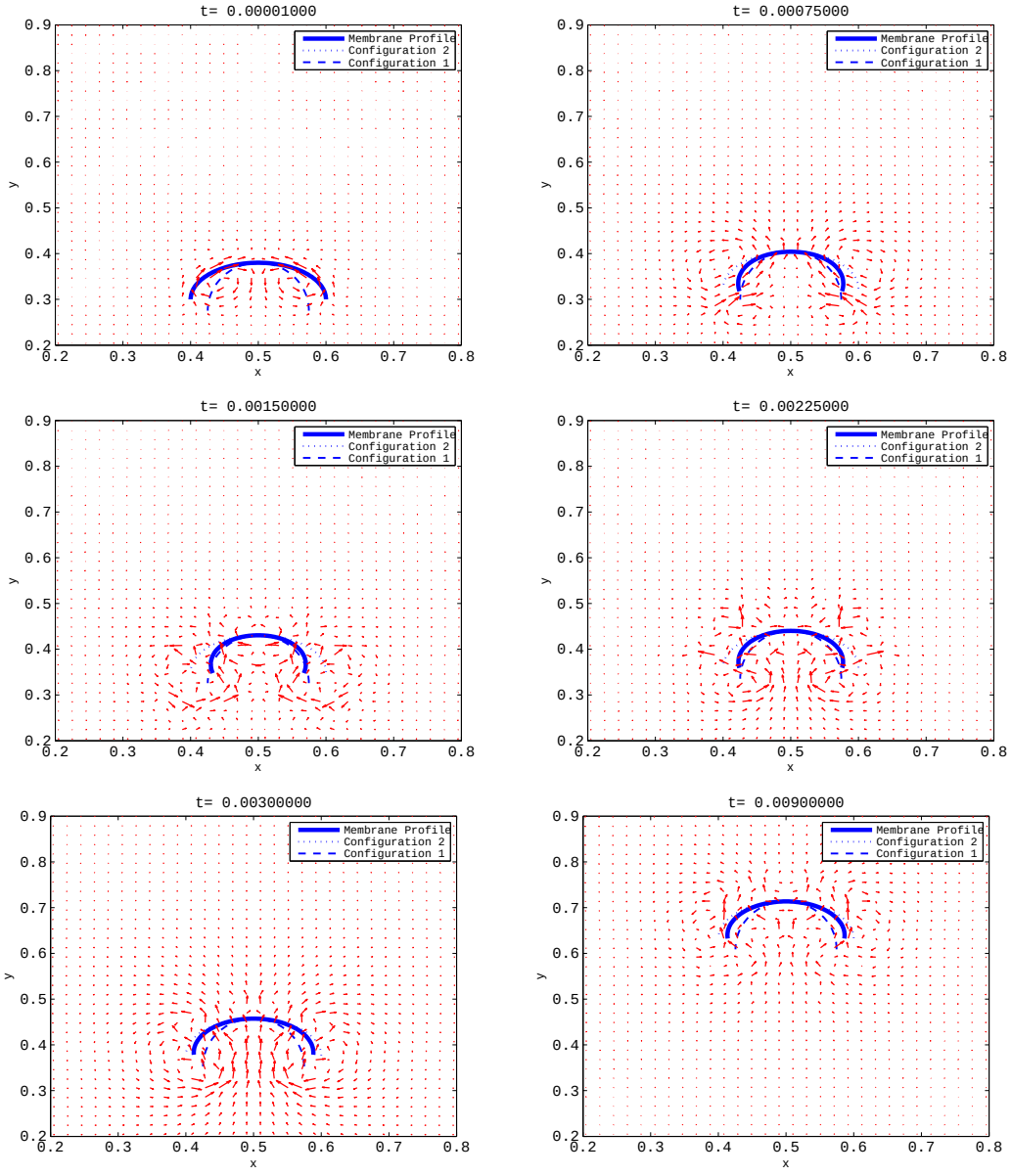

Figure 4.18: Time evolution of *Mitrocoma cellularia* in the simulation.

By comparing the dimensionless results in Table 4.1, the aspect ratio of the bell is clearly in the expected range, which means that the shape of the simulated bell is close to that in experiments. The average velocity is also in the expected range. The total displacement is close to the experimental data with a error around 10%, and our model is able to capture the "stair-step" shape in the displacement curve, which is very encouraging.The length of the bell oscillates around its resting length, within a relative tolerance of 12%, which indicates that there is not a significant change in the length. The jellyfish body contains fluid inside, and we expected that there would be some small changes in length when contracting the muscles.

We conclude that our IB model is capable of capturing the basic swimming dynamics of *Mitrocoma cellularia*, with a minimum of parameter fitting. There are two main aspect of our model that limit its applicability. First, the two dimensional geometry is not capable of capturing the true jetting/swimming behavior of a three dimensional hemispherical jellyfish bell. Secondly, *Mitrocoma cellularia* has a dense row of tentacles lining the entire edge of the bell that will obviously have some effect on the swimming behavior. These tentacles can not be incorporated in a two dimensional model, so we would have to extend our simulations to three dimensions in order to capture that effect.

4.3.6 Simulations of *Aequorea victoria*

These results motivated us to simulate *Aequorea victoria* with the same material properties and contraction force (constant σ_c), while only changing the aspect ratio and swimming frequency, due to the fact that they have similar size, and shape.

We simulate *Aequorea victoria* for the same time period as *Mitrocoma cellularia* which corresponds to six swimming periods, since the frequency is twice that of *Mitrocoma cellularia*. The results of simulations for *Aequorea victoria* are shown in the following figures. Figure 4.19 shows the length and aspect ratio, in which the length varies within 9.4% of the resting length and aspect ratio is in expected range. Figure 4.20 shows the displacement which shows a gradual increase without the "stair-stepping" seen in *Mitrocoma cellularia*. The corresponding plot of velocity is in Figure 4.21. Several snapshots of the shape of the bell are shown in Figure 4.22, and the comparison between simulation results and experimental data are listed in Table 4.1.

The simulation results indicate that the bell length and aspect ratio are in the expected range, as are the average velocity and displacement. As a result, our IB model is able to

capture the main feature of the dynamics of *Aequorea victoria* with only changes to the parameters governing muscle contraction frequency.

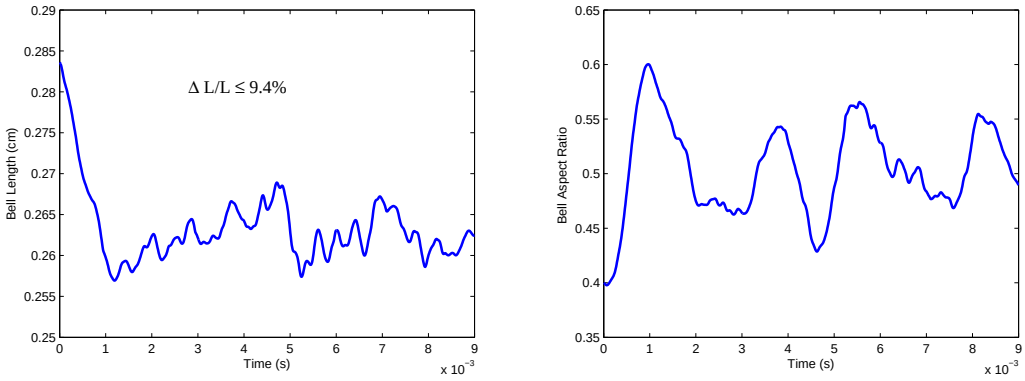

Figure 4.19: Bell length and aspect ratio of *Aequorea victoria*.

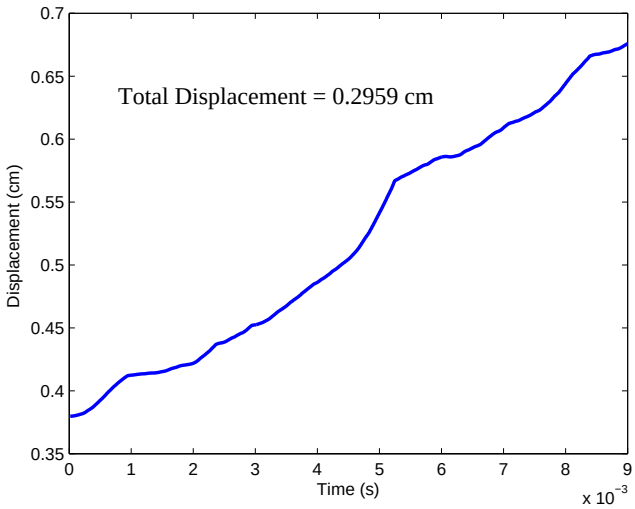

Figure 4.20: Displacement of *Aequorea victoria*.

4.4 Convergence Study

In this section, we perform a convergence study for parameters corresponding to *Mitrocoma cellularia* as listed in Table 4.1. We first consider a short period of time corresponding to a single recovery phase, and employ four grids with number of fluid points $N = 32$,

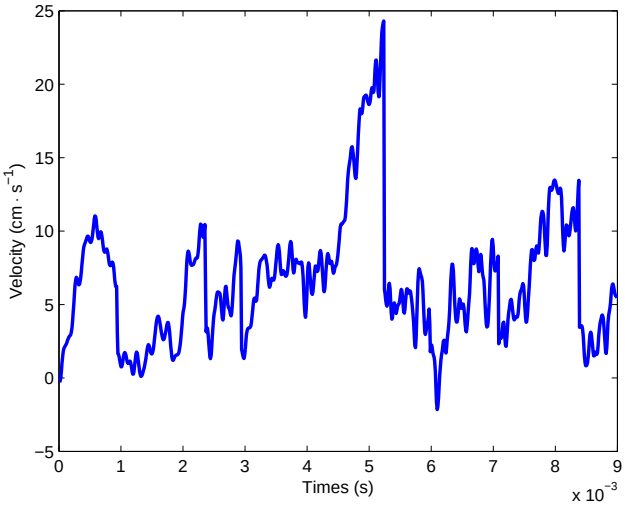

Figure 4.21: Velocity of *Aequorea victoria*.

64, 128 and 256, and a corresponding number of membrane points $N_b = 3N$. We plot in Figure 4.23 the differences in the velocity field between pairs of solutions on successive grids, measured in the 2-norm and max-norm. In relation to the "reference line" having slope 1, our results exhibit convergence at a rate slightly less than 1. This is consistent with theoretical results on convergence of the immersed boundary method by Mori [19], who proved that the method is first-order accurate in space owing to interpolation errors arising from using the approximate delta function.

We then perform a sequence of simulations over a much longer time period corresponding to several complete swimming cycles for *Mitrocoma cellularia*, and employ three grids with number of fluid points $N_1 = 32$, $N_2 = 64$ and $N_3 = 128$. First, we look at the convergence of the method for the case when the fiber grid is refined along with the fluid mesh according to $N_b = 3N_i$. The corresponding plots of velocity versus time are shown in Figure 4.24(a), where by "velocity" we mean the magnitude of the velocity at the IB point corresponding to the bell apex, which is most representative of the bell swimming velocity. The results for the two finest grids appear to have converged while the solution on the coarsest grid deviates significantly for times $t > 1 \times 10^{-3}$ s. We also repeated these simulations by maintaining the same fine fiber discretization $N_b = 3N_3$ for all three fluid grid resolutions N. The results for this simulation are pictured in Figure 4.24(b) where we observe that the coarse grid solution is much closer to that on the two finest grids. This supports the conclusion

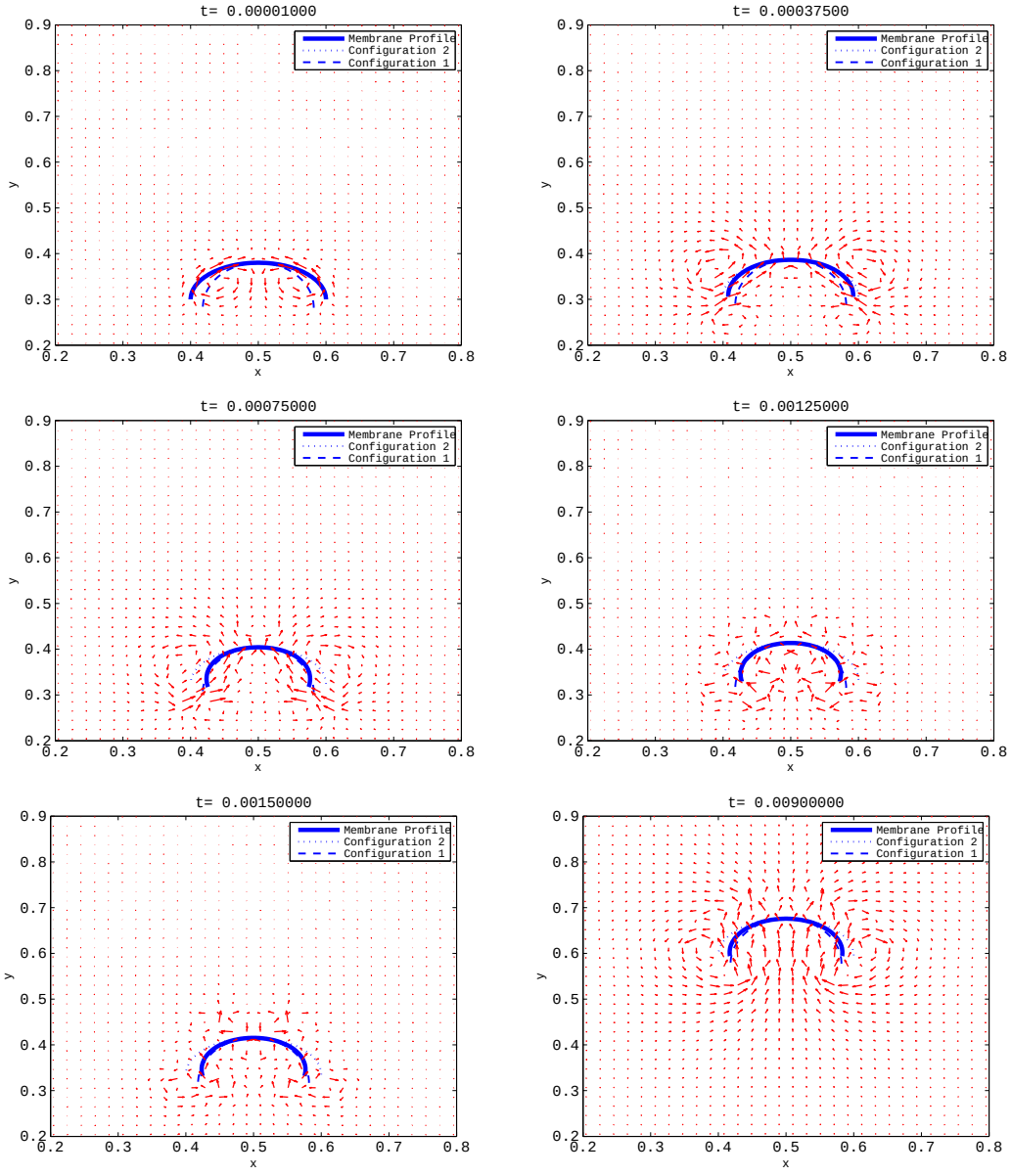

Figure 4.22: Time evolution of *Aequorea victoria* in the simulation.

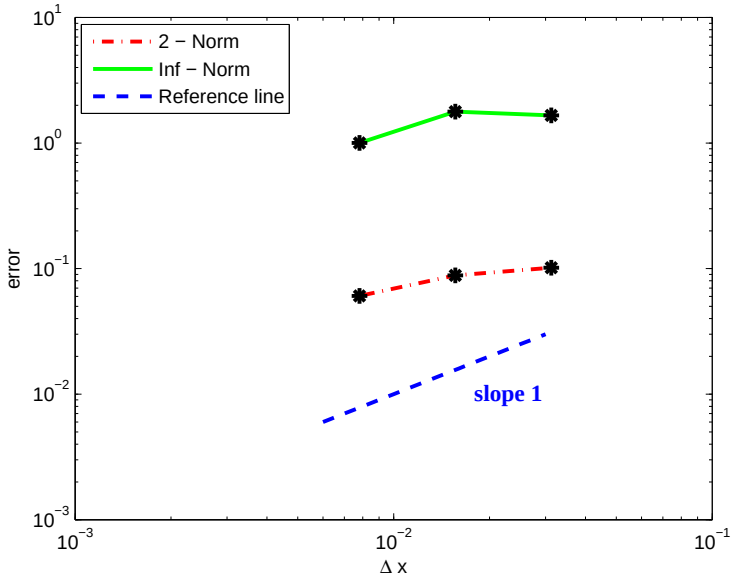

Figure 4.23: Convergence study for the recovery phase of *Mitrocoma cellularia*.

in [19] that the dominant source of error in the IB method is the interpolation errors on the immersed boundary.

4.4.1 Summary

The above two simulations of jellyfish species, *Mitrocoma cellularia* and *Aequorea victoria* indicate that our model generates continuous and stable swimming motions, and it is able to capture some key properties of the jellyfish swimming motion, such as aspect ratio, average velocity and displacement. The swimming motion of the bell emerges naturally from the fluid bell interaction, and requires only specification of structural and muscle contraction parameters that can be extracted from experimental measurements. The model does not specify the location or the configuration of the bell, and all the movements in the simulation are driven by elastic forces that are chosen to be as close as possible to the muscle contraction of actual jellyfish.

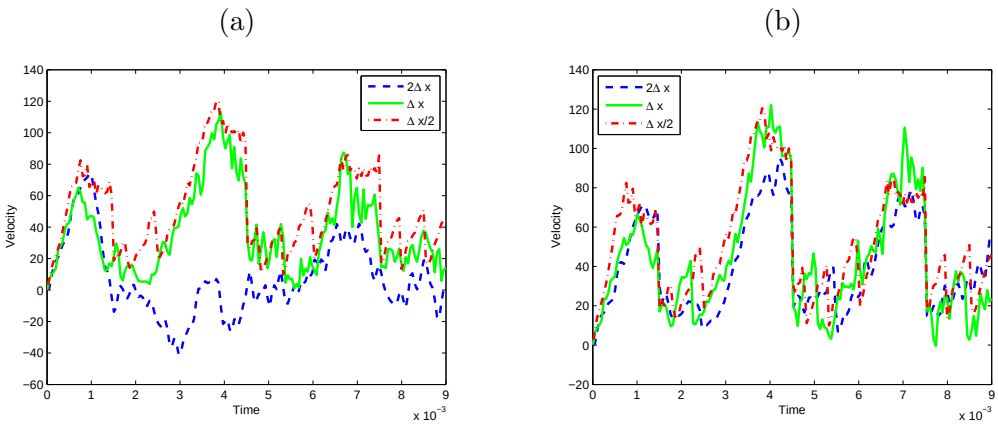

Figure 4.24: Convergence of the bell apex velocity on three fluid grids with $N_i = 32$, 64 and 128, and a fiber grid with (a) $N_b = 3N_i$, and (b) $N_b = \max_i N_i$.

Chapter 5

Conclusion

Our approach to simulating the swimming motion of a two dimensional jellyfish is based on using IB method to solve the Navier-Stokes equations in a square fluid domain with periodic boundary conditions. Our focus has been to use a simple bell model generated from experimental data to simulate the swimming motion of a two dimensional jellyfish without incorporating geometrical complexity. We also compare the emergent swimming dynamics of our model with experimental data, and we test our model with two different jellyfish species.

We begin by incorporating the bending force density into a closed membrane force calculation, and then test different combinations of stretching and bending forces. This reveals the relative importance of each force, and provides a better understanding of which force dominates the membrane motion according to the ratio of stretching stiffness over bending stiffness. The results motivate us to use an open membrane to represent the two dimensional configuration of a jellyfish. The membrane is modeled with stretching and bending stiffness, and the magnitudes of each are estimated based on experimental data from the literature. A periodic muscle contraction force is added at the end-points of the bell to simulate bell contractions, with the magnitude of the contraction force also estimated from experimental data. The swimming motion of our two dimensional jellyfish model is driven solely and naturally by the interaction between the fluid and bell, and the resulting dynamics are similar to swimming motions observed in experiments.

In the simulations for *Mitrocoma cellularia*, our model is able to capture the "stair-step" shape of the displacement and average velocity seen in experiments and the aspect ratio is also in the expected range. We then validate the model with simulations for another species,

Aequorea victoria, having similar size and shape.

This study opens up many areas for future research. First, there are several other species in [3] that we would like to simulate, especially those with large differences in size and shape, like *Aglantha digitale* and *Sarsia sp.*, as shown in Figure 5.1. Secondly, the simple one dimensional structure of the bell used here is probably too simple to fully capture the bending rigidity and muscle structure of an actual jellyfish, so we would like to incorporate a multi-layered, thick bell structure such as that used by [14]. Finally, our two dimensional bell misses many aspects of real jellyfish swimming dynamics seen in three dimensions. The geometrical limitations of a two dimensional geometry are obvious and so we would first implement a bell with a "round" or hemispherical shape. Moving up to three dimensions would also allow us to incorporate the effect of tentacles distributed along the bell periphery, which is a common feature in most jellyfish species.

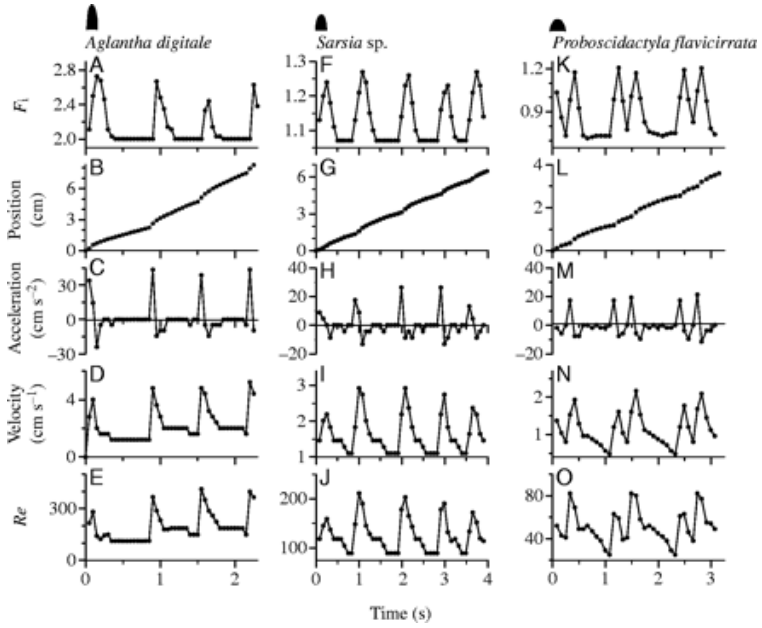

Figure 5.1: Experimental data for prolate jellyfish (*Aglantha digitale* and *Sarsia sp.*). Reprinted with permission of the *Journal of Experimental Biology* [3, Figs. 2].

Bibliography

[1] Michel Bergmann and Angelo Iollo. Modeling and simulation of fish-like swimming. *Journal of Computational Physics*, 230(2):329–348, 2011.

[2] Daniele Boffi, Lucia Gastaldi, and Luca Heltai. Numerical stability of the finite element immersed boundary method. *Mathematical Models and Methods in Applied Sciences*, 17(10):1479–1505, 2007.

[3] S.P. Colin and J.H. Costello. Morphology, swimming performance and propulsive mode of six co-occurring hydromedusae. *Journal of Experimental Biology*, 205(3):427–437, 2002. Available from: http://jeb.biologists.org/content/205/3/427.

[4] R. Cortez, L. Fauci, N. Cowen, and R. Dillon. Simulation of swimming organisms: coupling internal mechanics with external fluid dynamics. *Computing in Science & Engineering*, 6(3):38–45, 2004.

[5] R. Cortez, C.S. Peskin, J.M. Stockie, and D. Varela. Parametric resonance in immersed elastic boundaries. *SIAM Journal on Applied Mathematics*, 65(2):494–520, 2004.

[6] J.O. Dabiri, S.P. Colin, J.H. Costello, and M. Gharib. Flow patterns generated by oblate medusan jellyfish: Field measurements and laboratory analyses. *Journal of Experimental Biology*, 208(7):1257–1265, 2005.

[7] T. L. Daniel and M. S. Tu. Animal movement, mechanical tuning and coupled systems. *Journal of Experimental Biology*, 202:3415–3421, 1999.

[8] B.E. Griffith. On the volume conservation of the immersed boundary method. *Communications in Computational Physics*, 12(2):401–433, 2012.

[9] B.E. Griffith, X. Luo, D.M. McQueen, and C.S. Peskin. Simulating the fluid dynamics of natural and prosthetic heart valves using the immersed boundary method. *International Journal of Applied Mechanics*, 1(1):137–177, 2009.

[10] C. Hamlet. *Mathematical Modeling, Immersed Boundary Simulation, and Experimental Validation of the Fluid Flow around the Upside-Down Jellyfish Cassiopea xamachana.* PhD Thesis, Department of Mathematics, The University of North Carolina at Chapel Hill, 2011.

[11] C. Hamlet, L. A. Miller, T. Rodriguez, and A. Santhanakrishnan. In S. Childress, A. Hosoi, W. W. Schultz, and J. Wang, editors, *Natural Locomotion in Fluids and on Surfaces*, volume 155 of *The IMA Volumes in Mathematics and its Applications*, pages 35–51, 2012.

[12] C. Hamlet, A. Santhanakrishnan, and L.A. Miller. A numerical study of the effects of bell pulsation dynamics and oral arms on the exchange currents generated by the upside-down jellyfish *Cassiopea xamachana*. *Journal of Experimental Biology*, 214(11):1911–1921, 2011.

[13] G. Herschlag and L. Miller. Reynolds number limits for jet propulsion: A numerical study of simplified jellyfish. *Journal of Theoretical Biology*, 285(1):84–95, 2011.

[14] W. Huang and Y. J. Sung. An immersed boundary method for fluid-flexible structure interaction. *Computer Methods in Applied Mechanics and Engineering*, 198:2650–2661, 2009.

[15] J. Kim, D. Kim, and H. Choi. An immersed-boundary finite-volume method for simulations of flow in complex geometries. *Journal of Computational Physics*, 171(1):132–150, 2001.

[16] P. Lee, B. E. Griffith, and C. S. Peskin. The immersed boundary method for advection-electrodiffusion with implicit timestepping and local mesh refinement. *Journal of Computational Physics*, 229(13):5208–5227, 2010.

[17] M.J. McHenry and J. Jed. The ontogenetic scaling of hydrodynamics and swimming performance in jellyfish (*Aurelia aurita*). *Journal of Experimental Biology*, 206(22):4125–4137, 2003.

[18] W.M. Megill, J.M. Gosline, and R.W. Blake. The modulus of elasticity of fibrillin-containing elastic fibres in the mesoglea of the hydromedusa *Polyorchis penicillatus*. *Journal of Experimental Biology*, 208(20):3819–3834, 2005.

[19] Yoichiro Mori. Convergence proof of the velocity field for a stokes flow immersed boundary method. *Communications on Pure and Applied Mathematics*, 61(9):1213–1263, 2008.

[20] E.P. Newren. *Enhancing the immersed boundary method: stability, volume conservation, and implicit solvers*. PhD thesis, Department of Mathematics, The University of Utah, 2007.

[21] C.S. Peskin. The immersed boundary method. *Acta Numerica*, 11:479–517, 2002.

[22] C.S. Peskin and B.F. Printz. Improved volume conservation in the computation of flows with immersed elastic boundaries. *Journal of Computational Physics*, 105(1):33–46, 1993.

[23] D. Rudolf. Animating jellyfish through numerical simulation and symmetry exploitation. Master's thesis, Department of Computer Science, University of Saskatchewan, Saskatoon, August 2007.

[24] Mehmet Sahin and Kamran Mohseni. An arbitrary lagrangian–eulerian formulation for the numerical simulation of flow patterns generated by the hydromedusa *Aequorea victoria*. *Journal of Computational Physics*, 228(12):4588–4605, 2009.

[25] J.M. Stockie. *Analysis and computation of immersed boundaries, with application to pulp fibres*. PhD thesis, Department of Mathematics, University of British Columbia, 1997.

[26] Megan M Wilson, Jifeng Peng, John O Dabiri, and Jeff D Eldredge. Lagrangian coherent structures in low reynolds number swimming. *Journal of Physics: Condensed Matter*, 21(20):204105, 2009.

[27] Z. Yu. A DLM/FD method for fluid/flexible-body interactions. *Journal of Computational Physics*, 207(1):1–27, 2005.